REPORT DOCUMENTATION PAGE

Form Approved OMB NO. 0704-0188

1. REPORT DATE (DD-MM-YYYY)	2. REPORT TYPE	3. DATES COVERED (From - To)
13-05-2015	Final Report	8-Sep-2008 - 7-Sep-2014

4. TITLE AND SUBTITLE
Final Report: Novel Flame-Based Synthesis of Nanowires for Multifunctional Application

5a. CONTRACT NUMBER
W911NF-08-1-0417

5b. GRANT NUMBER

5c. PROGRAM ELEMENT NUMBER
611102

6. AUTHORS
Stephen D. Tse

5d. PROJECT NUMBER

5e. TASK NUMBER

5f. WORK UNIT NUMBER

7. PERFORMING ORGANIZATION NAMES AND ADDRESSES
Rutgers, The State University of New Jersey
Office Of Research & Sponsored Programs
58 Bevier Road
Piscataway, NJ 08854 -8010

8. PERFORMING ORGANIZATION REPORT NUMBER

9. SPONSORING/MONITORING AGENCY NAME(S) AND ADDRESS (ES)
U.S. Army Research Office
P.O. Box 12211
Research Triangle Park, NC 27709-2211

10. SPONSOR/MONITOR'S ACRONYM(S)
ARO

11. SPONSOR/MONITOR'S REPORT NUMBER(S)
52910-CH.11

12. DISTRIBUTION AVAILIBILITY STATEMENT
Approved for Public Release; Distribution Unlimited

13. SUPPLEMENTARY NOTES
The views, opinions and/or findings contained in this report are those of the author(s) and should not contrued as an official Department of the Army position, policy or decision, unless so designated by other documentation.

14. ABSTRACT
Progress for the project has been made in various areas. Specifically, we report on: (i) flame synthesis of metal-oxide nanowires and carbon nanotubes, (ii) evaporation-condensation synthesis of nanostructured tungsten oxide (WO2.9) fibers and discs, (iii) development of laser-based diagnostics for in-situ Raman characterization of as-synthesized nanomaterials, (iv) flame synthesis of graphene, (v) flame synthesis of metal-oxide porous films, (vi) development of low-intensity phase-selective laser-induced breakdown spectroscopy of nanomaterials, (vii) combined flame and electrodeposition synthesis of energetic coaxial WO2.9/Al nanowire arrays, and (viii)

15. SUBJECT TERMS
Nanowires, Nanoparticles, Graphene, Laser-based diagnostics

16. SECURITY CLASSIFICATION OF:			17. LIMITATION OF ABSTRACT	15. NUMBER OF PAGES	19a. NAME OF RESPONSIBLE PERSON
a. REPORT	b. ABSTRACT	c. THIS PAGE			Stephen Tse
UU	UU	UU	UU		19b. TELEPHONE NUMBER: 848-445-0449

Report Title

Final Report: Novel Flame-Based Synthesis of Nanowires for Multifunctional Application

ABSTRACT

Progress for the project has been made in various areas. Specifically, we report on: (i) flame synthesis of metal-oxide nanowires and carbon nanotubes, (ii) evaporation-condensation synthesis of nanostructured tungsten oxide (WO2.9) fibers and discs, (iii) development of laser-based diagnostics for in-situ Raman characterization of as-synthesized nanomaterials, (iv) flame synthesis of graphene, (v) flame synthesis of metal-oxide porous films, (vi) development of low-intensity phase-selective laser-induced breakdown spectroscopy of nanomaterials, (vii) combined flame and electrodeposition synthesis of energetic coaxial WO2.9/Al nanowire arrays, and (viii) sequential flame and solution synthesis of tungsten-oxide and zinc/tin-oxide nanoheterostructures.

Enter List of papers submitted or published that acknowledge ARO support from the start of the project to the date of this printing. List the papers, including journal references, in the following categories:

(a) Papers published in peer-reviewed journals (N/A for none)

Received		Paper
01/27/2013	5.00	Li Shuiqing, Sili Deng, Qiang Yao, Yiyang Zhang, Stephen D. Tse. Direct synthesis of nanostructured TiO2 films with controlled morphologies by stagnation swirl flames, Journal of Aerosol Science, (02 2012): 71. doi: 10.1016/j.jaerosci.2011.10.001
01/28/2013	6.00	Nasir K. Memon, Stephen D. Tse, Manish Chhowalla, Bernard H. Kear. Role of substrate, temperature, and hydrogen on the flame synthesis of graphene films, Proceedings of the Combustion Institute, (01 2013): 2163. doi: 10.1016/j.proci.2012.06.112
05/13/2015	7.00	Yiyang Zhang, Gang Xiong, Shuiqing Li, Zhizhong Dong, Steven G. Buckley, Stephen D. Tse. Novel low-intensity phase-selective laser-induced breakdown spectroscopy of TiO2 nanoparticle aerosols during flame synthesis, , (03 2013): 0. doi: 10.1016/j.combustflame.2012.11.007
05/13/2015	9.00	Bernard H. Kear, Stephen D. Tse, Nasir K. Memon. Transition between graphene-film and carbon-nanotube growth on Nickel alloys in open-atmosphere flame synthesis, Chemical Physics Letters, (05 2013): 90. doi: 10.1016/j.cplett.2013.03.046
05/13/2015	10.00	Zhizhong Dong, Jafar F. Al-Sharab, Bernard H. Kear, Stephen D. Tse. Combined Flame and Electrodeposition Synthesis of Energetic Coaxial Tungsten-Oxide/Aluminum Nanowire Arrays, Nano Letters, (09 2013): 4346. doi: 10.1021/nl4021446
05/13/2015	8.00	Fusheng Xu, Geliang Sun, Sage J.B. Dunham, Bernard H. Kear, Stephen D. Tse, Nasir K. Memon. Flame synthesis of carbon nanotubes and few-layer graphene on metal-oxide spinel powders, Carbon, (11 2013): 478. doi: 10.1016/j.carbon.2013.07.023
12/20/2012	1.00	J. F. Al-Sharab, R. K. Sadangi, V. Shukla, S. D. Tse, B. H. Kear. Synthesis of Nanostructured Tungsten Oxide (WO2.9) Fibers and Discs, Crystal Growth & Design, (11 2009): 4680. doi: 10.1021/cg900544k
12/20/2012	2.00	X. Liu, M. E. Smith, S. D. Tse. In situ Raman characterization of nanoparticle aerosols during flame synthesis, Applied Physics B, (06 2010): 643. doi: 10.1007/s00340-010-4091-x
12/28/2012	4.00	Nasir K. Memon, Stephen D. Tse, Jafar F. Al-Sharab, Hisato Yamaguchi, Alem-Mar B. Goncalves, Bernard H. Kear, Yogesh Jaluria, Eva Y. Andrei, Manish Chhowalla. Flame synthesis of graphene films in open environments, Carbon, (12 2011): 5064. doi: 10.1016/j.carbon.2011.07.024
TOTAL:		**9**

Number of Papers published in peer-reviewed journals:

(b) Papers published in non-peer-reviewed journals (N/A for none)

Received	Paper

TOTAL:

Number of Papers published in non peer-reviewed journals:

(c) Presentations

1. Xu, F., D'Esposito, C., Liu, X., Kear, B.H., and Tse, S.D., "Flame Synthesis of ZnO Nanostructures: Morphology and Local Growth Conditions," Poster presentation, Published in Conference Proceedings, 1142-JJ05-39, Materials Research Society Fall Meeting, Dec 3, 2008, Boston, MA.

2. Tse, S.D., D'Esposito, C., Xu, F., Liu, X., Al-Sharab, J.F., and Kear, B.H., "Flame Synthesis of Tungsten Oxide Nanostructures: Morphology and Local Growth Conditions," Sub-Micron and Nanostructured Ceramics, Engineering Conferences International, Jun 7-12, 2009, Colorado Springs, CO.

3. Al-Sharab, J.F., Sadangi, R.K., Kear, B.H., and Tse, S.D., "Vapor Synthesis of Tungsten Oxide Nanofibers," Sub-Micron and Nanostructured Ceramics, Engineering Conferences International, Jun 7-12, 2009, Colorado Springs, CO.

4. D'Esposito, C., Al-Sharab, J., Kear, B.H., and Tse, S.D., "Non-Catalytic Flame Synthesis of Carbon Nanotubes," Poster-presentation, Materials Research Society Fall Meeting, Nov 30 - Dec 4, 2009, Boston, MA.

5. Memon, N., Al-Sharab, J.F., Jaluria, Y., Kear, B.H., and Tse, S.D., "Scalable Flame Synthesis of Carbon Nanotubes on Substrates," Materials Research Society Fall Meeting, Nov 29 - Dec 3, 2010, Boston, MA.

6. Dong. Z., Di, Huo, Kear, B.H., and Tse, S.D., "Combined Flame and Solution Synthesis of Hetero-junction Nanowires," Poster-presentation, Materials Research Society Fall Meeting, Nov 29 - Dec 3, 2010, Boston, MA.

7. Memon, N., Al-Sharab, J.F., Jaluria, Y., Kear, B.H., Chhowalla, M., and Tse, S.D., "Flame Synthesis of Nanostructured Carbon," 2011-TPC-1232, The Twenty-First (2011) International Offshore (Ocean) and Engineering Conference, Jun 19-24, 2011, Maui, HI.

8. Memon, N., Tse, S.D., Chhowalla, M., Kear, B., Jaluria, Y., "Flame Synthesis of Few-Layer Graphene," ASME International Mechanical Engineering Congress Conference, Nov 11 - 17, 2011, Denver, CO.

9. Memon, N., Tse, S.D., Al-Sharab, J.F., Yamaguchi, H., Jaluria, Y., Kear, B.H., Chhowalla, M., "Novel Flame Synthesis of Graphene Films," Materials Research Society Fall Meeting, Nov 28 - Dec 2, 2011, Boston, MA.

10. Memon, N.K., Tse, S.D., Chhowalla, M., Kear, B.H., "Role of substrate, temperature, and hydrogen on the flame synthesis of graphene films," 1G08, 34th International Symposium on Combustion, The Combustion Institute, 29 Jul - Aug 3, 2012, Warsaw University of Technology, Warsaw, Poland.

11. Memon, N.K., Tse, S.D., Chhowalla, M., Kear, B.H., "Flame synthesis of graphene films: Effects of substrate composition, temperature and hydrogen addition," XI International Conference on Nanostructured Materials, Aug 26-31, 2012, Rhodes, Greece.

12. Memon, N., Dunham, S., Kear, B.H., Tse, S.D., "Flame Synthesis of Graphene and Carbon Nanotubes on Metal-oxide Spinels," Materials Research Society Fall Meeting, Nov 25-30, 2012, Boston, MA.

13. Dong, Z., Al-sharab, J.F., Kear, B.H., Tse, S.D., "Core/shell WO2.9/Al Nanowires for Nano-energetic Applications," Poster-presentation, Materials Research Society Fall Meeting, Nov 25-30, 2012, Boston, MA.

14. Tse, S.D., Dong, Z., Kear, B., Al-Sharab, J., "Coaxial Tungsten-Oxide/Aluminum Thermite Nanocomposite," SES 50th Annual Technical Meeting and ASME-AMD Annual Summer Meeting, July 28-31, 2013, Brown University, Providence, RI.

15. Mozet, W., Tse, S.D., Kear, B., Cheong, S.W., "Pulsed Laser Deposition of Carbon Nanomaterials," IMECE2013-66826, ASME 2013 International Mechanical Engineering Congress and Exposition, Nov 15-21, 2013, San Diego, CA.

16. Dong, Z., Kear, B., Tse, S.D., "Fabrication of Energetic MoO2/Al Core/Shell Nanoplates," IMECE2013-66828, ASME 2013 International Mechanical Engineering Congress and Exposition, Nov 15-21, 2013, San Diego, CA.

17. Hong, H., Tse, S.D., "Combustion-Assisted CVD Synthesis of Monolayer Graphene Films in Open-Atmosphere Environments," Poster-Presentation, RR7.01, 2013 Materials Research Society Fall Meeting & Exhibit, Dec 1-6, 2013, Boston, MA.

18. Mozet, W., Tse, S.D., "Pulsed Laser Deposition of Carbon Nanomaterials," Poster-Presentation, RR7.15, 2013 Materials Research Society Fall Meeting & Exhibit, Dec 1-6, 2013, Boston, MA.

19. Dong, Z., Al-Sharab, J., Kear, B.H., Tse, S.D., "Metal-Oxide/Aluminum Coaxial Nanowires for Nano-Energetic Applications," Poster-Presentation, SS19.105, 2013 Materials Research Society Fall Meeting & Exhibit, Dec 1-6, 2013, Boston, MA.

20. Tse, S.D., "Combined Flame and Solution Synthesis of Nanoheterostructures," Invited Talk, Techconnect World Innovation conference & Expo (Nanotech 2014), Jun 15-18, 2014, Washington, D.C.

21. Mozet, W.T., Tse, S.D., Kear, B.H., Chhowalla, M., Cheong, S.W., “Pulsed Laser Deposition of Carbon Nanomaterials,” Techconnect World Innovation conference & Expo (Nanotech 2014), Jun 15-18, 2014, Washington, D.C.

Number of Presentations: 21.00

Non Peer-Reviewed Conference Proceeding publications (other than abstracts):

Received Paper

TOTAL:

Number of Non Peer-Reviewed Conference Proceeding publications (other than abstracts):

Peer-Reviewed Conference Proceeding publications (other than abstracts):

Received Paper

TOTAL:

Number of Peer-Reviewed Conference Proceeding publications (other than abstracts):

(d) Manuscripts

Received Paper

TOTAL:

Number of Manuscripts:

Books

Received Book

TOTAL:

Received Book Chapter

TOTAL:

Patents Submitted

Novel Low Intensity Phase-Selective Laser-Induced Breakdown Spectroscopy of Nanoparticles

Patents Awarded

Awards

2014 Rutgers Board of Trustees Award for Excellence in Research (2013-2014), "For his numerous path-breaking contributions to the areas of combustion technology, nanofibers, and nanomaterials, including his pioneering use of innovative laser diagnostic tools to probe the combustion-flame environment leading to a fundamental understanding of combustion-synthesis dynamics,"

Graduate Students

NAME	PERCENT_SUPPORTED	Discipline
Nasir Memon	0.00	
Zhizhong Dong	0.25	
Cassandra D'Esposito	0.00	
Xiaofei Liu	0.00	
FTE Equivalent:	**0.25**	
Total Number:	**4**	

Names of Post Doctorates

NAME	PERCENT_SUPPORTED
Gang Xiong	0.25
Geliang Sun	0.25
FTE Equivalent:	**0.50**
Total Number:	**2**

Names of Faculty Supported

NAME	PERCENT_SUPPORTED	National Academy Member
Stephen Tse	0.10	
FTE Equivalent:	**0.10**	
Total Number:	**1**	

Names of Under Graduate students supported

NAME	PERCENT_SUPPORTED
FTE Equivalent:	
Total Number:	

Student Metrics

This section only applies to graduating undergraduates supported by this agreement in this reporting period

The number of undergraduates funded by this agreement who graduated during this period: 0.00

The number of undergraduates funded by this agreement who graduated during this period with a degree in science, mathematics, engineering, or technology fields:..... 0.00

The number of undergraduates funded by your agreement who graduated during this period and will continue to pursue a graduate or Ph.D. degree in science, mathematics, engineering, or technology fields:..... 0.00

Number of graduating undergraduates who achieved a 3.5 GPA to 4.0 (4.0 max scale):..... 0.00

Number of graduating undergraduates funded by a DoD funded Center of Excellence grant for Education, Research and Engineering:..... 0.00

The number of undergraduates funded by your agreement who graduated during this period and intend to work for the Department of Defense 0.00

The number of undergraduates funded by your agreement who graduated during this period and will receive scholarships or fellowships for further studies in science, mathematics, engineering or technology fields:..... 0.00

Names of Personnel receiving masters degrees

NAME	
Cassandra D'Esposito	
Total Number:	**1**

Names of personnel receiving PHDs

NAME	
Nasir Memon	
Zhizhong Dong	
Xiaofei Liu	
Total Number:	**3**

Names of other research staff

NAME	PERCENT_SUPPORTED
FTE Equivalent:	
Total Number:	

Sub Contractors (DD882)

Inventions (DD882)

Scientific Progress

See Attachment

Technology Transfer

N/A

Project Summary - Grant # (W911NF-08-1-0417)
(Final Report: September 2014)

Novel Flame-Based Synthesis of Nanowires for Multifunctional Application

Stephen D. Tse
Department of Mechanical and Aerospace Engineering
Rutgers University, Piscataway, NJ, 08854

Objective
The objective of the project was to increase fundamental understanding of the mechanisms of nanowire formation and growth in flames, and utilization of that understanding to define process conditions that enable high-rate and high-purity synthesis of nanostructures with tailored compositions, crystallinities, and morphologies (e.g. wires, rods, ribbons, films, etc).

Approach
The program integrates synthesis, in-situ laser-based diagnosis, and subsequent characterization to optimize metal-oxide nanowire growth using strategic combustion geometries, doping, ambient pressure effects, and electric-field process control. The integrated primary research components are to:

- Conduct experiments in strategic and aerodynamically simple flow fields, i.e. flat-flame stagnation-point (premixed) and flat-flame counterflow (non-premixed) configurations, to characterize the effects of fuel composition, flame temperature, inert addition, hydrogen addition, oxygen concentration, strain rate, pressure, and other controllable process parameters on nano-rod/wire properties;
- Synthesize metal-oxide nanowires, i.e. Al_2O_3, SnO_2, ZnO, MoO_3, CuO, WO_3, Fe_2O_3, Bi_2O_3, and MnO_2
- Perform doping studies (with In, Sn, and Sb) for the ZnO and SnO_2 systems;
- Investigate the influence of electric fields to control nanowire purity, growth rate, and morphology;
- Utilize in-situ laser-based diagnostics, including spontaneous Raman spectroscopy (SRS) and laser-induced fluorescence (LIF), to determine the gas-phase chemical species concentrations and temperature distribution in the regions near the probe/substrate conducive for nano-rod/wire growth. Laser Doppler Velocimetry (LDV) will be used to determine the local strain rate;
- Characterize the nano-rod/wire characteristics using field emission scanning electron microscopy (FESEM), with EDX, and high resolution transmission electron microscopy (HRTEM), with SAED.
- Simulate growth conditions corresponding to the experiments employing modified flame codes with detailed gas-phase and surface chemical kinetics and transport.

Relevance to Army
Robust materials with improved properties are needed for structural, functional, and device applications in the U.S. Army. Of strong interest are functional one-dimensional nanostructures due to their unique and innovative applications in optics, optoelectronics, catalysis, and piezoelectricity. Semiconducting oxide nanowires constitute a unique group of 1D nanomaterials, which have well-defined and uniform shapes, stable surfaces, and single-crystal volumes. These properties are keys to nanoelectronic applications like use as field effect transistors, ultra-sensitive nano-size gas sensors, nanoresonators, and nanocantilevers. Moreover, nanowires of MoO_3, CuO, WO_3, Fe_2O_3, Bi_2O_3, and MnO_2 can be exploited for tailored heat release in nano-energetic applications involving thermite reactions with nano-Al.

Accomplishments for Reporting Period

Progress for the project has been made in various areas. Specifically, we report on: (*i*) flame synthesis of metal-oxide nanowires and carbon nanotubes, (*ii*) evaporation-condensation synthesis of nanostructured tungsten oxide ($WO_{2.9}$) fibers and discs, (*iii*) development of laser-based diagnostics for in-situ Raman characterization of as-synthesized nanomaterials, (*iv*) flame synthesis of graphene, (*v*) flame synthesis of metal-oxide porous films, (*vi*) development of low-intensity phase-selective laser-induced breakdown spectroscopy of nanomaterials, (*vii*)

combined flame and electrodeposition synthesis of energetic coaxial $WO_{2.9}$/Al nanowire arrays, and (*viii*) sequential flame and solution synthesis of tungsten-oxide and zinc/tin-oxide nanoheterostructures.

Collaborations and Technology Transfer
N/A

Resulting Journal Publications during Reporting Period

1. Al-Sharab, J.F., Sadangi, R.K., Shukla, V., Tse, S.D., and Kear, B.H., "Synthesis of Nanostructured Tungsten Oxide ($WO_{2.9}$) Fibers and Discs," *Crystal Growth and Design* **9**:4680-4684 (2009).
2. Liu, X., Smith, M.E., and Tse, S.D., "In-situ Raman Characterization of Nanoparticle Aerosols during Flame Synthesis," *Applied Physics B: Lasers and Optics* **100**(3):643-653 (2010).
3. Memon, N.K., Tse, S.D., Al-Sharab, J., Yamaguchi, H., Goncalves, A.B., Kear, B.H., Jaluria, Y., Andrei, E.Y., and Chhowalla, M., "Flame Synthesis of Graphene Films in Open-Environments," *Carbon* **49**:5064-5070 (2011).
4. Zhang, Y., Li, S., Deng, S., Yao, Q., and Tse, S.D., "Direct Synthesis of Nanostructured TiO_2 Films with Controlled Morphology by a Stagnation Swirl Flame," *Journal of Aerosol Science* **44**:71-82 (2012).
5. Zhang, Y., Xiong, G., Li, S., Dong, Z., Buckley, S.G., and Tse, S.D., "Novel Low-Intensity Phase-Selective Laser-Induced Breakdown Spectroscopy of TiO_2 Nanoparticle Aerosols during Flame Synthesis," *Combustion and Flame* **160**:725-733 (2013).
6. Memon, N.K., Tse, S.D., Chhowalla, M., and Kear, B.H., "Role of Substrate, Temperature, and Hydrogen on the Flame Synthesis of Graphene Films," *Proceedings of the Combustion Institute* **34**:2163-2170 (2013).
7. Memon, N.K., Xu, F., Sun, G., Dunham, S., Kear, B.H., and Tse, S.D., "Flame Synthesis of Carbon Nanotubes and Few-Layer Graphene on Metal-Oxide Spinel Powders," *Carbon* **63**:478-486 (2013).
8. Memon, N.K., Kear, B.H., and Tse, S.D., "Transition from Carbon-Nanotube to Graphene-Film Growth on Nickel Alloys in Open-Atmosphere Flame Synthesis," *Chemical Physics Letters* **570**:90-94 (2013).
9. Dong, Z., Al-Sharab, J.F., Kear, B.H., and Tse, S.D., "Combined Flame and Electrodeposition Synthesis of Energetic Coaxial Tungsten-Oxide/Aluminum Nanowire Arrays," *Nano Letters* **13**(9):4346-4350 (2013).

Conference papers/presentations

1. Xu, F., D'Esposito, C., Liu, X., Kear, B.H., and Tse, S.D., "Flame Synthesis of ZnO Nanostructures: Morphology and Local Growth Conditions," Poster presentation, Published in Conference Proceedings, 1142-JJ05-39, *Materials Research Society Fall Meeting*, Dec 3, 2008, Boston, MA.
2. Tse, S.D., D'Esposito, C., Xu, F., Liu, X., Al-Sharab, J.F., and Kear, B.H., "Flame Synthesis of Tungsten Oxide Nanostructures: Morphology and Local Growth Conditions," *Sub-Micron and Nanostructured Ceramics*, Engineering Conferences International, Jun 7-12, 2009, Colorado Springs, CO.
3. Al-Sharab, J.F., Sadangi, R.K., Kear, B.H., and Tse, S.D., "Vapor Synthesis of Tungsten Oxide Nanofibers," *Sub-Micron and Nanostructured Ceramics*, Engineering Conferences International, Jun 7-12, 2009, Colorado Springs, CO.
4. D'Esposito, C., Al-Sharab, J., Kear, B.H., and Tse, S.D., "Non-Catalytic Flame Synthesis of Carbon Nanotubes," Poster-presentation, *Materials Research Society Fall Meeting*, Nov 30 - Dec 4, 2009, Boston, MA.
5. Memon, N., Al-Sharab, J.F., Jaluria, Y., Kear, B.H., and Tse, S.D., "Scalable Flame Synthesis of Carbon Nanotubes on Substrates," *Materials Research Society Fall Meeting*, Nov 29 - Dec 3, 2010, Boston, MA.
6. Dong. Z., Di, Huo, Kear, B.H., and Tse, S.D., "Combined Flame and Solution Synthesis of Hetero-junction Nanowires," Poster-presentation, *Materials Research Society Fall Meeting*, Nov 29 - Dec 3, 2010, Boston, MA.
7. Memon, N., Al-Sharab, J.F., Jaluria, Y., Kear, B.H., Chhowalla, M., and Tse, S.D., "Flame Synthesis of Nanostructured Carbon," 2011-TPC-1232, *The Twenty-First (2011) International Offshore (Ocean) and Engineering Conference*, Jun 19-24, 2011, Maui, HI.
8. Memon, N., Tse, S.D., Chhowalla, M., Kear, B., Jaluria, Y., "Flame Synthesis of Few-Layer Graphene," *ASME International Mechanical Engineering Congress Conference*, Nov 11 - 17, 2011, Denver, CO.
9. Memon, N., Tse, S.D., Al-Sharab, J.F., Yamaguchi, H., Jaluria, Y., Kear, B.H., Chhowalla, M., "Novel Flame Synthesis of Graphene Films," *Materials Research Society Fall Meeting*, Nov 28 - Dec 2, 2011, Boston, MA.

10. Memon, N.K., Tse, S.D., Chhowalla, M., Kear, B.H., "Role of substrate, temperature, and hydrogen on the flame synthesis of graphene films," 1G08, *34th International Symposium on Combustion*, The Combustion Institute, 29 Jul - Aug 3, 2012, Warsaw University of Technology, Warsaw, Poland.
11. Memon, N.K., Tse, S.D., Chhowalla, M., Kear, B.H., "Flame synthesis of graphene films: Effects of substrate composition, temperature and hydrogen addition," *XI International Conference on Nanostructured Materials*, Aug 26-31, 2012, Rhodes, Greece.
12. Memon, N., Dunham, S., Kear, B.H., Tse, S.D., "Flame Synthesis of Graphene and Carbon Nanotubes on Metal-oxide Spinels," *Materials Research Society Fall Meeting*, Nov 25-30, 2012, Boston, MA.
13. Dong, Z., Al-sharab, J.F., Kear, B.H., Tse, S.D., "Core/shell $WO_{2.9}$/Al Nanowires for Nano-energetic Applications," Poster-presentation, *Materials Research Society Fall Meeting*, Nov 25-30, 2012, Boston, MA.
14. Tse, S.D., Dong, Z., Kear, B., Al-Sharab, J., "Coaxial Tungsten-Oxide/Aluminum Thermite Nanocomposite," *SES 50th Annual Technical Meeting and ASME-AMD Annual Summer Meeting*, July 28-31, 2013, Brown University, Providence, RI.
15. Mozet, W., Tse, S.D., Kear, B., Cheong, S.W., "Pulsed Laser Deposition of Carbon Nanomaterials," IMECE2013-66826, *ASME 2013 International Mechanical Engineering Congress and Exposition*, Nov 15-21, 2013, San Diego, CA.
16. Dong, Z., Kear, B., Tse, S.D., "Fabrication of Energetic MoO_2/Al Core/Shell Nanoplates," IMECE2013-66828, *ASME 2013 International Mechanical Engineering Congress and Exposition*, Nov 15-21, 2013, San Diego, CA.
17. Hong, H., Tse, S.D., "Combustion-Assisted CVD Synthesis of Monolayer Graphene Films in Open-Atmosphere Environments," Poster-Presentation, RR7.01, *2013 Materials Research Society Fall Meeting & Exhibit*, Dec 1-6, 2013, Boston, MA.
18. Mozet, W., Tse, S.D., "Pulsed Laser Deposition of Carbon Nanomaterials," Poster-Presentation, RR7.15, *2013 Materials Research Society Fall Meeting & Exhibit*, Dec 1-6, 2013, Boston, MA.
19. Dong, Z., Al-Sharab, J., Kear, B.H., Tse, S.D., "Metal-Oxide/Aluminum Coaxial Nanowires for Nano-Energetic Applications," Poster-Presentation, SS19.105, *2013 Materials Research Society Fall Meeting & Exhibit*, Dec 1-6, 2013, Boston, MA.
20. Tse, S.D., "Combined Flame and Solution Synthesis of Nanoheterostructures," Invited Talk, *Techconnect World Innovation conference & Expo (Nanotech 2014)*, Jun 15-18, 2014, Washington, D.C.
21. Mozet, W.T., Tse, S.D., Kear, B.H., Chhowalla, M., Cheong, S.W., "Pulsed Laser Deposition of Carbon Nanomaterials," *Techconnect World Innovation conference & Expo (Nanotech 2014)*, Jun 15-18, 2014, Washington, D.C.

Graduate Students Involved During Reporting Period

- Nasir Memon (Ph.D. student)
- Zhizhong Dong (Ph.D. student)
- Xiaofei Liu (Ph.D. student)
- Cassandra D'Esposito (M.S. student)

Post-Doc Involved During Reporting Period

- Dr. Gang Xiong
- Dr. Geliang Sun

Awards, Honors and Appointments

- 2014 Rutgers Board of Trustees Award for Excellence in Research (2013-2014), "For his numerous path-breaking contributions to the areas of combustion technology, nanofibers, and nanomaterials, including his pioneering use of innovative laser diagnostic tools to probe the combustion-flame environment leading to a fundamental understanding of combustion-synthesis dynamics,"

- 07/2012, Promotion to Full Professor, Department of Mechanical and Aerospace Engineering, Rutgers, the State University of New Jersey; Piscataway, NJ 08854
- 09/2009, Appointed Co-Director, Center for Nanomaterials Research, Rutgers, the State University of New Jersey; Piscataway, NJ 08854

Report on Accomplishments

1. Flame Synthesis of Metal-Oxide Nanowires and Carbon Nanotubes (CNTs)

Below are summaries of the materials synthesized. A draft manuscript is being prepared for submission to a journal for publication.

Tungsten Oxide Nanowires

Various WO_x nanostructures are produced from counter-flow diffusion flames (CDFs), which allow for correlation of morphologies with local conditions due to the quasi-one-dimensionality of the flow field. The CDF setup consists of two converging nozzles with a 15-mm separation distance, which can be seen in Fig. 1(a). Computational simulations allow the chemical species to be tailored in the flame structure. The synthesis is carried out at one atmosphere pressure using tungsten metal substrates, which can be placed on either the air side or fuel side of the reaction zone, permitting evaluation of the roles of H_2O (or CO_2) versus O_2 in the synthesis of WO_x nanostructures. Furthermore, methane flames are compared with hydrogen flames, which only have H_2O (and no CO_2) as product species. The temperature profiles of the methane and hydrogen flames are strategically matched in order to compare chemical species. Figures 1(a) and (b) show graphs of the temperature and species concentrations of the two flame structures obtained by computational simulations using GRI-Mech 1.2, which, although not shown, are verified using spontaneous Raman spectroscopy (SRS). In all the experiments, the gas-phase temperature is ~1720K. On the air side of the flames, the substrate temperature is ~1600K; and on the fuel side, it is ~1550K.

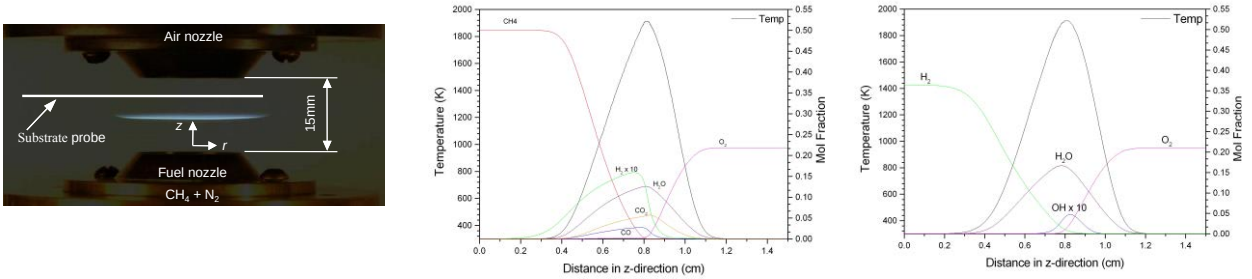

(a) Experimental setup, showing substrate probe on the air side of the reaction zone.

(b) Methane-based flame: temperature and major species profiles

(c) Methane-based flame: temperature and major species profiles.

Figure 1. Counterflow synthesis flame setup.

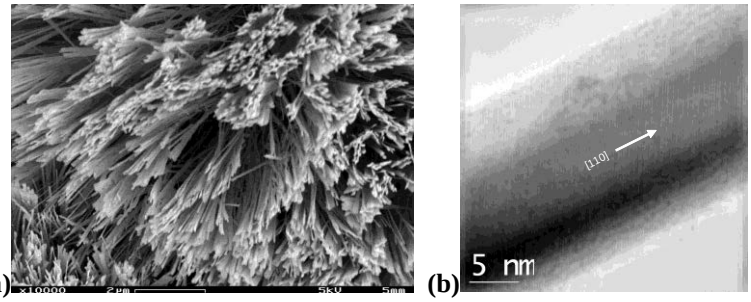

(a) **(b)**

Figure 2. FESEM and HRTEM images of nanowires grown on the air side of the methane-based flame.

Probing on the air side of the methane flame, chemical routes involving O_2, CO_2, and H_2O exist, to produce a dense yield of well aligned nanowires that have diameters of 20-50nm with lengths > 10μm for a sampling duration of 10min, grown directly on the tungsten substrate, Fig. 2(a). Analysis of the two-dimensional Fourier transform pattern of the TEM image gives an average spacing for the lattice planes of 3.78 Å, which corresponds to the reflections from *d*-spacings of (110) planes of the tetragonal $WO_{2.9}$ phase. Thus, these as-grown single-crystalline nanowires have preferable growth along the [110] direction, as indicated in Fig. 2(b).

Since all of the nanowires are $WO_{2.9}$ from core to surface, we conclude that hydrogen reduction occurs in the gas phase, producing gas-phase $WO_{2.9}$, which then condenses to form $WO_{2.9}$ nanowires that grow in length by a tip-accretion mechanism and thicken by a ledge-growth mechanism, as revealed by TEM imaging. Thus, a likely mechanism for the O_2 route is:

$W^{(s)} + 1.5\ O_2^{(g)} \rightarrow WO_3^{(g)}$, ΔG = -198.5 kJ/mol at 1700K,

$WO_3^{(g)} + 0.1\ H_2^{(g)} \rightarrow WO_{2.9}^{(s)} + 0.1\ H_2O^{(g)}$, ΔG = -225.5 kJ/mol at 1700K.

For the H_2O route, hydrate species formation and "gas-phase" hydrogen reduction is a possible mechanism, i.e.:

$W^{(s)} + 4\ H_2O^{(g)} \rightarrow WO_2(OH)_2^{(g)} + 3\ H_2^{(g)}$ ΔG = >0 kJ/mol at 1700K,

$WO_2(OH)_2^{(g)} + 0.1\ H_2^{(g)} \rightarrow WO_{2.9}^{(s)} + 1.1\ H_2O^{(g)}$ ΔG = -38.4 kJ/mol at 1700K.

However, as seen above, the first step is not favorable. Yet, tungsten-oxide is known to photocatalytically convert H_2O to OH. Reaction of W(s) with OH would then be favorable in producing gas-phase tungsten hydrate species. This is currently being investigated in detail using direction illumination during synthesis. For the CO_2 route, gas-phase formation does not appear to be favorable, e.g.:

$W^{(s)} + 3\ CO_2^{(g)} \rightarrow WO_3^{(g)} + 3CO^{(g)}$ ΔG = +208 kJ/mol at 1700K.

Instead, it can play an important role in *seeding* nanowire formation through a heterogeneous route,

$W^{(s)} + 2.9\ CO_2^{(g)} \rightarrow WO_{2.9}^{(g)} + 2.9\ CO^{(g)}$ ΔG = -15.8 kJ/mol at 1700K,

whereby subsequent nanowire growth then proceeds from either the O_2 or H_2O routes.

Probing on the fuel side of the methane flame, chemical routes involving CO_2 and H_2O (but no O_2) exist, to produce a dense yield of nanowires, Fig. 3. However, these nanowires are not as well aligned as those produced on the air side, Fig. 2, but also have diameters 20-50nm, with somewhat shorter lengths of > 2μm, for the same sampling duration. TEM imaging and SAED, Fig. 3, confirm that the nanowires are tetragonal $WO_{2.9}$, but the growth direction is now [200], different than that for the air side [110].

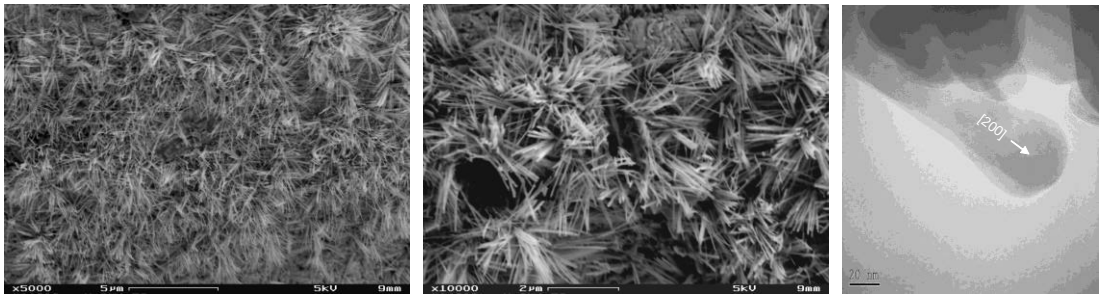

Figure 3. FESEM and TEM images of nanowires grown on the fuel side of the methane-based flame.

Probing on the fuel side of the hydrogen flame isolates the H_2O chemical route (no CO_2 or O_2). Figure 4 shows a sparse yield of unaligned nanowires that are much larger in characteristic diameter (< 150nm) than those produced in the methane flames. The lengths are ~5μm in length, versus 10μm for the methane-air side. TEM imaging and SAED, Fig. 4, again confirm the tetragonal $WO_{2.9}$ phase, but the nanowire growth direction is now [101], different than the previous two cases.

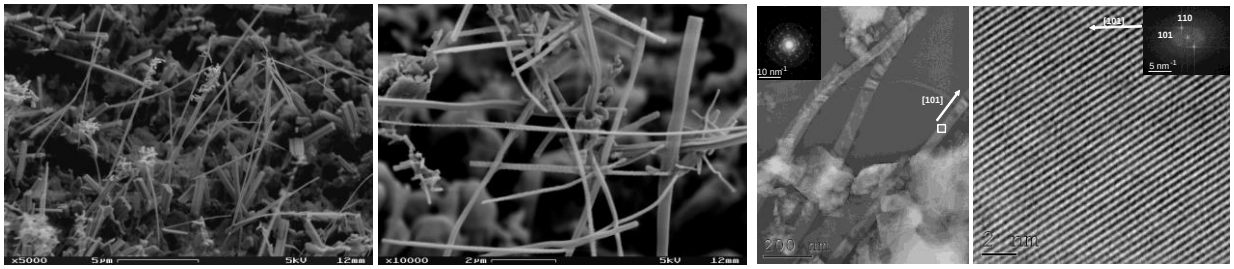

Figure 4. FESEM and HRTEM images of nanowires grown on the fuel side of the hydrogen-based flame.

Probing on the air side of the hydrogen flame allows for investigation of the H_2O and O_2 (no CO_2) chemical routes. The result is a somewhat sparse yield of unaligned nanowires that are even larger in characteristic diameter (< 200nm), though as long as those produced on the methane air-side (> 10μm), Fig. 5. The nanowires exhibit tetragonal $WO_{2.9}$ crystal structure, as confirmed with SAED and HRTEM analyses, Fig. 5. As observed from the diffraction pattern, the wires grow as single crystals with preferable growth orientation along the <110> direction, similar to nanowires synthesized on the air-side of the methane flame. In some cases, branching at 90° is observed, as shown in Fig. 5, due to similar *d*-spacing between perpendicular (110) and (-110).

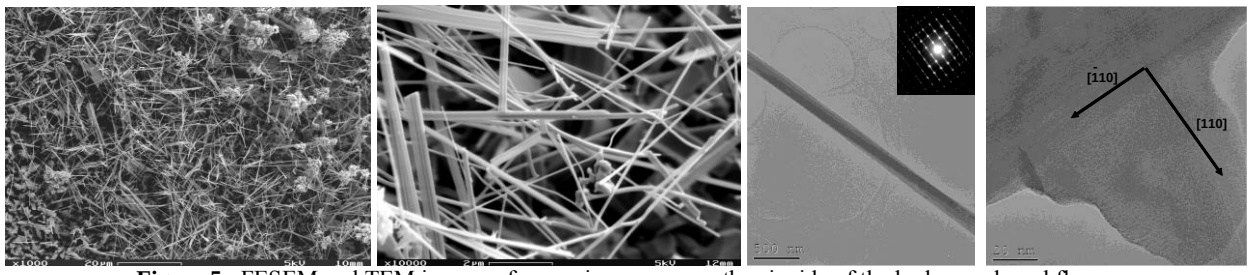

Figure 5. FESEM and TEM images of nanowires grown on the air side of the hydrogen-based flame.

There is no doubt that H_2 plays in an important role. For all the cases, except that for the hydrogen flame probed on the air side, small concentrations of H_2 are inherently present at the probe location (see Fig. 1), which, in combination with the elevated temperatures, can aid in initial nanoparticle formation. Moreover, as evidenced by the proposed chemical routes for $WO_{2.9}$ nanowire formation, gas-phase hydrogen reduction is necessary to form the sub-oxide in the gas phase. However, for the case of the hydrogen flame probed on the air side, no H_2 is provided by the flame reactions as seen in Fig. 1, which is needed for the reactions involving the O_2 and H_2O chemical routes. Nonetheless, inspection of the H_2O chemical route divulges that H_2 is produced in the reaction of tungsten with water vapor. Thus, H_2O presence is needed in this case for the oxygen route to proceed.

Interestingly, no tungsten carbide nanowire formation is found in our investigations, despite favorable Gibbs free energy calculations for the reactions. The activation energy, which controls the kinetic rates, is probably much larger for the associated tungsten carbide reactions, contributing to why tungsten oxide is the preferred growth structure. In other works, tungsten carbide is found to form only when substrate temperatures are above 1673K, supporting the activation energy argument. In our experiments, the substrate temperatures are between 1550K and 1600K. As a result, although carbide induced breakup of the substrate surface likely plays a role in initial formation of nucleation sites (including that for tungsten oxide) for our cases, no subsequent carbide nanowire growth occurs.

In this project, comparisons of nanostructures synthesized between methane and hydrogen flames allows for assessment of the respective roles of H_2O versus CO_2 versus O_2 on WO_x morphology and composition. We evince that O_2 is not necessary to produce the nanowires. Although the H_2O route is isolated and shown to produce nanowires, it is not very efficient, in terms of yield or quality. A combination of O_2, H_2O, and CO_2 routes seem to produce optimum growth, where the heterogeneous CO_2 route aids considerably in seeding nanowire growth.

Zinc Oxide Nanostructures

Zinc can be oxidized by interactions with water vapor, carbon dioxide, and oxygen, all of which are present in a methane diffusion flame. In this work, ZnO nanostructures are synthesized in methane and hydrogen diffusion flames to isolate growth mechanisms and perform a parametric study of local growth conditions. A zinc-plated steel probe is inserted into a counterflow diffusion flame (CDF) at various axial distances in order to correlate morphologies with local growth conditions. We demonstrate the growth of ZnO nanostructures at 1000, 1300, and 1600K (see Figs. 6 and 7). Growth appears to be a vapor-liquid-solid mechanism, with key parameters being radical species present, oxidizer, carbon dioxide, and water vapor concentrations, substrate temperature, and gas-phase temperature.

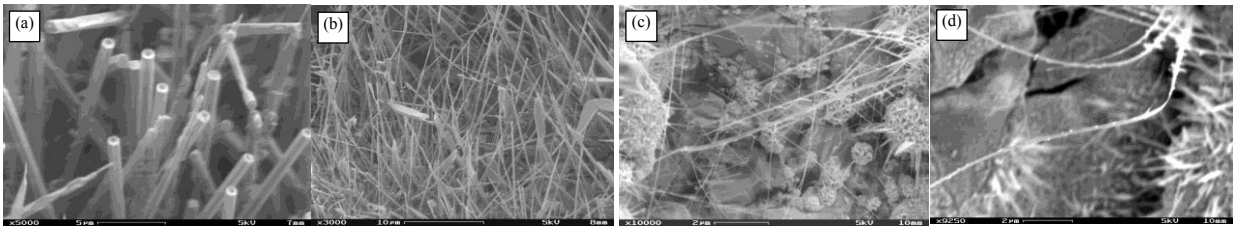

Figure 6. ZnO nanomaterials from the fuel side of the methane flame. (a) T = 1600 K, (b) T = 1300 K, (c) and (d) T = 1000 K.

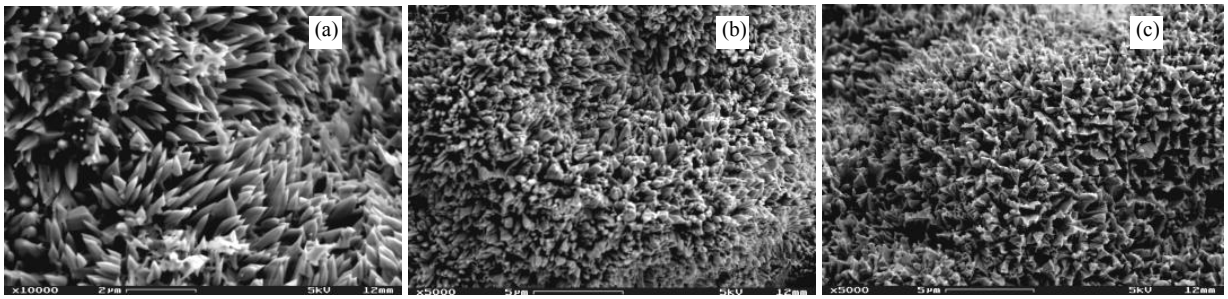

Figure 7. ZnO nanomaterials grown in the hydrogen flame at (a) 1600 K, (b) 1300 K, and (c) 1000 K.

Molybdenum Oxide Nanoplates

On the air side of the methane flame, molybdenum-oxide (MoO_2) nanoplates are formed. The nanoplates, shown in Figure 8(a) and (b), are a few hundred nanometers wide, about 50nm thick, and about one micron in length. On the fuel side of the methane flame, smaller nanoplates are grown than on the air side. In **Error! Reference source not found.** 8(c) it can be seen that there is a large coverage density of molybdenum oxide on the substrate surface; and in **Error! Reference source not found.**(d), it can be seen that the width and length of the nanoplates are less than 100nm and 1 micron, respectively.

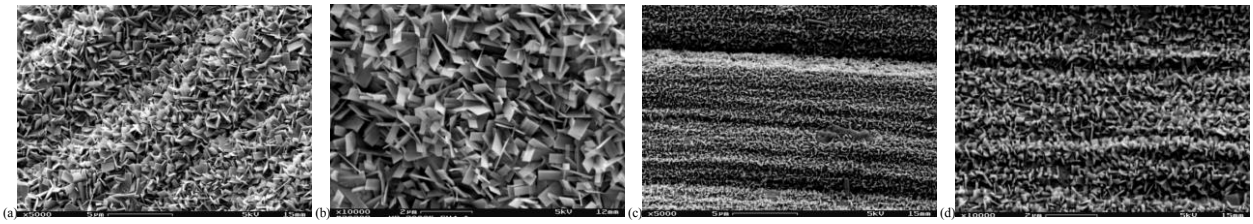

Figure 8. Molybdenum oxide nanoplates grown in the CH_4 flame on the air side (z=+.83cm) at (a) low magnification (b) and high magnification. Molybdenum oxide nanoplates grown in the CH_4 flame on the fuel side (z=+0.79cm) at (c) low magnification (d) and high magnification.

Copper Oxide Nanowires

Cu_2O nanowires are grown only on the air side of the flames with the densest yield in the methane flame. Figure 9 show a dense yield of copper oxide nanowires grown at ~900K in the methane flame. The nanowires are approximately 150nm in diameter and a few microns in length.

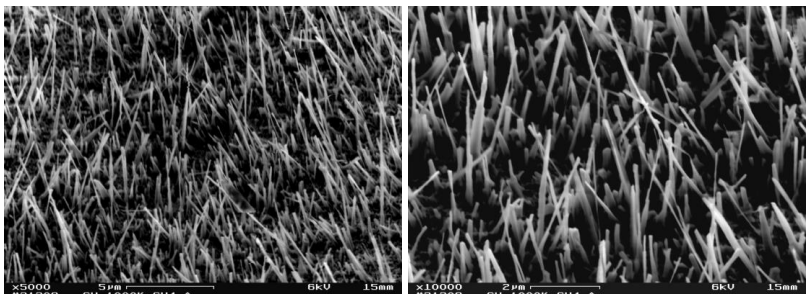

Figure 9. (a) Low magnification copper oxide nanowires grown in a CH_4 flame (z=+0.97cm) (b) Magnified FESEM image of nanowires grown in CH_4

Iron Oxide Nanowires

A dense yield of Fe_3O_4 nanowires are grown on the air side of the methane and hydrogen diffusion flames at ~1000K. The fuel side results show some oxidation of the iron as well as carbon nanotube growth. Figure 10(a) shows iron oxide nanowires grown on the air side of the methane flame. The wires are about 150nm in diameter and a few microns in length. Iron oxide nanowires are also grown in the hydrogen flame, as seen in **Error! Reference source not found.**. 10(b). They are ~200nm in diameter and a few microns in length.

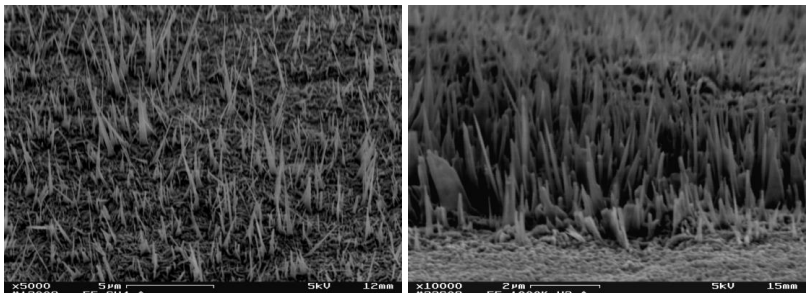

Figure 10. Iron oxide nanowires grown in (a) CH_4 flame (b) H_2 flame.

Non-Catalytic Flame Synthesis of Carbon Nanotubes

Using the counterflow diffusion flame configuration of Fig. 1, with a tungsten substrate inserted on the fuel side of a methane flame (Fig. 1(b)), carbon nanotubes (CNTs) are synthesized without the use of catalysts, presumably due to the high temperatures involved the combustion flow field (versus that for conventional CVD). Figure 11(a) shows the CNTs deposited on the substrate. Figure 11(b) divulges that the CNTs are MWNTs. Fig. 11(c) shows the presence of nano-onions. Some of the TEM images suggest the presence of graphene as well; see Fig. 11(d). These results are presently being verified using Raman Spectroscopy.

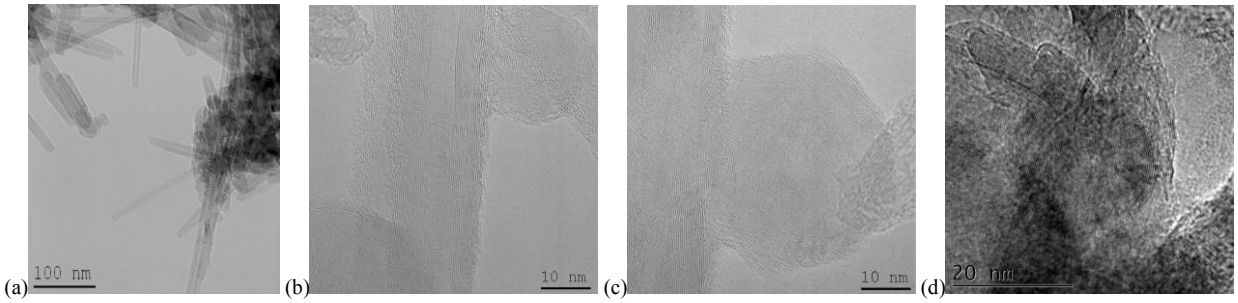

Figure 11. (a) TEM showing CNTs, (b) HRTEM of MWNTs, (c) HRTEM of nano-onions, (d) HRTEM showing possible graphene.

2. Evaporation-Condensation Synthesis of Nanostructured Tungsten Oxide ($WO_{2.9}$) Fibers and Discs

Evaporation of $WO_{3.0}$ powder during transmission electron microscopy resulted in the formation of nanofibers of $WO_{2.9}$, which deposited on adjacent cooler regions of the carbon substrate. Controlled experiments using the inert gas condensation (IGC) method were performed to investigate the formation mechanism of the nanofibers. Depending on the growth conditions, different morphologies of $WO_{2.9}$ phase were observed. Structural characterization was carried out using analytical electron microscopy techniques. All the morphologies observed in these experiments have [110] growth direction. HRTEM imaging of the faceting of single crystal nanodiscs permitted an estimation of the relative surface energies. On the basis of these observations, a qualitative growth model is proposed. Details of this work have been published and are found in [Pub. 1, Al-Sharab et al., *Crystal Growth and Design*, 2009].

3. Development of Laser-based Diagnostics for In-situ Raman Characterization of As-synthesized Nanomaterials

Raman spectroscopy is applied to diagnose nanoparticle presence and characteristics in a gaseous flow field. Specifically, in situ monitoring of the Raman-active modes of TiO_2 and Al_2O_3 nanoparticles in aerosol form is demonstrated in high-temperature flame environments. This technique serves as a sensitive and reliable way to characterize particle composition and crystallinity and delineate the phase conversion of nanoparticles as they evolve in the flow field. The effect of temperature on the solid-particle Raman spectra is investigated by seeding nanoparticles into a co-flow jet diffusion flame, where local gas-phase temperatures are correlated by shape-fitting the N_2 vibrational Stokes Q-branch Raman spectra. Applying the technique to a flame synthesis environment, the results demonstrate that in situ Raman of as-formed nanoparticles can be readily applied to other gas-phase synthesis systems, especially as an on-line diagnostic. Details of this work have been published and are found in [Pub. 2, Liu

et al., *Applied Physics B: Lasers and Optics*, 2010]. Nanoparticle diagnosis was the first step in developing this technique for the in-situ characterization of nanowires during flame synthesis.

4. Flame synthesis of Graphene

Functionalized graphene may not only act as a stabilizer for reactive metal nanoparticles, providing a significant energy barrier, but also offers catalytic sites to control the combustion of the nano-energetics As such, research in to flame-synthesized graphene has been conducted

Few-layer graphene is grown on copper and nickel substrates at high rates using a novel flame synthesis method in open-atmosphere environments. Transmittance and resistance properties of the transferred films are similar to those grown by other methods, but the concentration of oxygen, as assessed by X-ray photoelectron spectroscopy, is actually less than that for graphene grown by chemical vapor deposition under near vacuum conditions. The method involves utilizing a multi-element inverse-diffusion-flame burner, where post-flame species and temperatures are radially-uniform upon deposition at a substrate. Advantages of the specific flame synthesis method are scalability for large-area surface coverage, increased growth rates, high purity and yield, continuous processing, and reduced costs due to efficient use of fuel as both heat source and reagent. Additionally, by adjusting local growth conditions, other carbon nanostructures (i.e. nanotubes) are readily synthesized. Details of this work have been published and are found in [Pub. 3, Memon et al., *Carbon*, 2011].

Graphene films are grown in open-atmosphere on metal substrates using a multiple inverse-diffusion flame burner with methane as fuel. Substrate material (i.e. copper, nickel, cobalt, iron, and copper–nickel alloy), along with its temperature and hydrogen treatment, strongly impacts the quality and uniformity of the graphene films. The growth of few-layer graphene (FLG) occurs in the temperature range 750–950ºC for copper and 600–850ºC for nickel and cobalt. For iron, the growth of graphene is not exclusively observed. The variation of graphene quality for different substrates is believed to be due primarily to the difference in carbon solubility between the metals. Details of this work have been published and are found in [Pub. 6, Memon et al., *Proceedings of the Combustion Institute*, 2013].

Multi-walled and single-walled carbon nanotubes (CNTs) and few-layer graphene (FLG) are grown directly on spinel powders using flame synthesis. CNT and FLG growth occurs via the decomposition of flame-generated carbon precursors (e.g., CO, C_2H_2, and CH_4) over nanoparticles (i.e., Ni, Co, Fe, and Cu) reduced from the solid oxide. The growth of CNTs is investigated on $NiAl_2O4$, $CoAl_2O_4$, and $ZnFe_2O_4$, using counterflow diffusion flame and multiple inverse-diffusion flames (m-IDFs), while the growth of FLG is investigated on CuFe2O4 using m-IDFs. As shown by analytical electron microscopy techniques, Raman spectroscopy, and X-ray diffraction, substrate temperature and spinel composition play critical roles in the growth of both CNTs and FLG. Details of this work have been published and are found in [Pub. 7, Memon et al., *Carbon*, 2013].

Using open-atmosphere flame synthesis, graphene films and carbon nanotubes (CNTs) are grown directly on nickel and nickel-alloy substrates. The gas-flow input CH_4 to H_2 ratio (1:10) is held constant. For nickel, copper–nickel, and Inconel, few-layer graphene (FLG) grows at 850ºC. Transitional growth from FLG to CNTs is observed on nickel, copper–nickel, and Inconel, as the substrate temperature is decreased to 500ºC. CNT growth is found for nitinol at 500ºC; however, graphene growth is not observed for nitinol at elevated temperatures for the examined experimental conditions. Details of this work have been published and are found in [Pub. 8, Memon et al., *Chemical Physics Letters*, 2013].

5. Flame synthesis of Metal-Oxide Porous Films

A novel premixed swirl flame in stagnation point geometry is used to synthesize uniform, high-quality nanostructured TiO_2 films at growth rates of 20–200 nm/s in a single step. The roles of precursor concentration and substrate temperature in controlling film morphology and characteristics are investigated. Increasing precursor concentration, for a given substrate temperature, significantly increases the packing density of the nanoporous film. The specific surface area of the film is mainly dependent on substrate temperature, where two distinct regimes, i.e. in-flame-agglomeration at low temperature and on-substrate-sintering at high temperature, specify film properties. A simplified deposition model for the formation of the nanoporous film structure is proposed, correlating penetration distance of thermophoretically-driven Brownian particles into the film with the resultant morphology. The model predicts the packing density in excellent agreement with experiments, thereby clarifying the complex roles of precursor concentration and substrate temperature. Finally, increasing substrate temperature, at fixed precursor concentration, changes the packing density little, but considerably decreases specific surface area, as sintering becomes dominant among controlling mechanisms. Details of this work have been published and are

found in [Pub. 4, Zhang et al., *Journal of Aerosol Science*, 2012]. Nanoparticle films was the first step in developing this technique, and nanowire films are currently being investigated.

6. Development of Low-Intensity Phase-Selective Laser-Induced Breakdown Spectroscopy of Nanomaterials

Novel low-intensity laser-induced breakdown spectroscopy (LIBS) is employed to conduct an in situ study on swirl flame synthesis of TiO_2 nanoparticles. Collected emissions agree well with Ti atomic spectra from the NIST database. In contrast to traditional application of LIBS on particles, the power used here is much lower (~35 mJ/pulse or 28 J/cm^2 at 532 nm); and no macroscopic spark is visually observed. Nevertheless, the low-intensity LIBS shows interesting selectivity—only exciting Ti atoms in particle phase, with no breakdown emission occurring for gas molecules (e.g. titanium tetraisopropoxide precursor, air). The emission intensity increases as the nanoparticles grow in the synthesis flow field, plateauing as the particles become larger than 6 nm, indicating the absorption efficiency to be size-dependent for small particles. The signals saturate at a fluence of ~16 J/cm2. When the precursor concentration is larger than 150 ppm (corresponding to particle sizes of 6–8 nm), the emission intensity increases linearly with precursor concentration. The selectivity of the low-intensity LIBS for such application could be advantageous for tracking nanoparticle formation and for measuring particle volume fraction during gas-phase synthesis or other systems. The size-dependent absorption efficiency could be used to measure nanoparticle size in situ. Details of this work have been published and are found in [Pub. 5, Zhang et al., *Combustion and Flame*, 2013]. Nanoparticle diagnosis was the first step in developing this technique for the in-situ characterization of nanowires during flame synthesis.

Low-intensity phase-selective laser induced breakdown spectroscopy (LIBS) with secondary resonant excitation from the same single laser pulse is employed in the *in-situ* study of flame synthesis of TiO_2 nanoparticles. Excitation from the third harmonic (i.e. 354.71 nm as measured) of an injection-seeded Nd:YAG laser breaks down flame-synthesized titanium-dioxide nanoparticles in-situ into their elements and then subsequently excites the titanium electrons resonantly. With low-intensity laser excitation (~30 mJ/pulse or 60 J/cm^2), only the nanoparticle phase is selectively broken down, forming nano-plasmas without any observable plasma Bremsstrahlung radiation. The induced emission at 497.534 nm resulting from the secondary resonant excitation is markedly stronger than other/primary emissions. Compared to 532 nm excitation (with no secondary resonant excitation), with saturation at a laser power of ~20 mJ/pulse, the emissions from 354.71 nm excitation exhibit no saturation with laser power, until gas-phase breakdown. Temporal evolutions of the emissions are also studied, revealing that the 497.534 nm emission peaks earlier, but does not last as long as the other emissions. Emission peak splitting and dependence on excitation laser wavelength are observed and investigated, respectively. Using the secondary resonant excitation effect, phase-selective measurements of nano-aerosol characteristics can be made at improved detection thresholds. Details of this work have been included in a draft manuscript to be submitted to a journal for publication, as found in Attachment A.

7. Combined Flame and Electrodeposition Synthesis of Energetic Coaxial $WO_{2.9}$/Al Nanowire Arrays

A nanostructured thermite composite comprising an array of tungsten-oxide ($WO_{2.9}$) nanowires (diameters of 20−50 nm and lengths of >10 μm) coated with single crystal aluminum (thickness of ∼16 nm) has been fabricated. The method involves combined flame synthesis of tungsten-oxide nanowires and ionic-liquid electrodeposition of aluminum. The geometry not only presents an avenue to tailor heat release characteristics due to anisotropic arrangement of fuel and oxidizer but also eliminates or minimizes the presence of an interfacial Al_2O_3 passivation layer. Upon ignition, the energetic nanocomposite exhibits strong exothermicity, thereby being useful for fundamental study of aluminothermic reactions as well as enhancing combustion characteristics. Details of this work have been published and are found in [Pub. 9, Dong et al., *Nano Letters*, 2013].

8. Sequential Flame and Solution Synthesis of Tungsten-Oxide and Zinc/Tin-Oxide Nanoheterostructures

Several new kinds of heterostructures of $WO_{2.9}$ nanowires with ZnO/SnO_2 nanostructures have been synthesized via a combined flame and solution synthesis method. First, vertically well-aligned single-crystal tungsten-oxide nanowires are grown directly on a tungsten substrate via a flame synthesis method. Here, $WO_{2.9}$ nanowires are produced by the vapor-solid (VS) mechanism, with gas phase species (O_2, H_2O, CO_2, and H_2) and local gas phase temperature (1720K) specified at the substrate for desired growth, e.g. diameters of 20-50nm, lengths > 10μm, and coverage density of 10^9-10^{10}cm^{-2}. Then, various kinds of ZnO/SnO_2 nanostructures are grown on the $WO_{2.9}$ nanowires by adjusting the concentration ratio of Zn^{2+} and Sn^{2+} in an aqueous ethylenediamine solution. With $WO_{2.9}$ nanowires serving as the scaffold, sequential growth of hexagonal ZnO nanoplates, Zn_2SnO_4 nanocubes, and

SnO_2 nanoparticles are attained for Zn^{2+}:Sn^{2+} ratios of 1:0, 10:1, and 1:10, respectively. High-resolution transmission electron microscopy (HRTEM) of the interfaces at the nanoheterojunctions show atomically abrupt interfaces for $ZnO/WO_{2.9}$ and $Zn_2SnO_4/WO_{2.9}$, despite lattice mismatches of >20%. The process demonstrated in this work might provide a rapid, readily scaled, and versatile synthesis route for development of functional nanoheterostructures. Details of this work have been included in a draft manuscript to be submitted to a journal for publication, as found in Attachment B.

Attachment A

Draft Manuscript

Phase-selective laser-induced breakdown spectroscopy of nanoparticle aerosols with secondary resonant excitation during flame synthesis

Gang Xiong[1], Shuiqing Li[2], Yiyang Zhang[3], Steven G. Buckley[4], and Stephen D. Tse[1*]

[1]Department of Mechanical and Aerospace Engineering, Rutgers, The State University of New Jersey, Piscataway, NJ 08854, USA

[2]Department of Thermal Engineering, Tsinghua University, Beijing 100084, China

[3]Institute of Nuclear and New Energy Technology, Tsinghua University, Beijing 100084, China

[4]TSI, Inc., Redmond, WA 98052, USA

*corresponding author: sdytse@rci.rutgers.edu

Abstract

Novel low-intensity phase-selective laser induced breakdown spectroscopy (LIBS) with secondary resonant excitation from the same single laser pulse is employed in the *in-situ* study of flame synthesis of TiO_2 nanoparticles. Excitation from the third harmonic (i.e. 354.71 nm as measured) of an injection-seeded Nd:YAG laser breaks down flame-synthesized titanium-dioxide nanoparticles in-situ into their elements and then subsequently excites the titanium electrons resonantly. With low-intensity laser excitation (~30 mJ/pulse or 24 J/cm^2), only the nanoparticle phase is selectively broken down, forming nano-plasmas without any observable plasma Bremsstrahlung radiation. The induced emission at 497.534 nm resulting from the

secondary resonant excitation is markedly stronger than other/primary emissions. Compared to 532 nm excitation (with no secondary resonant excitation), with saturation at a laser power of ~20 mJ/pulse (16 J/cm^2 fluence) the emissions from 354.71 nm excitation exhibit no saturation with laser power due to the secondary resonant excitation, until gas-phase breakdown. Temporal evolutions of the emissions are also studied, revealing that the 497.534 nm emission peaks earlier, but does not last as long as the other emissions. Emission peak splitting and dependence on excitation laser wavelength are observed and investigated, respectively. Using the secondary resonant excitation effect, phase-selective measurements of nano-aerosol characteristics can be made at improved detection thresholds.

Key words: resonant laser induced breakdown spectroscopy (LIBS); phase selective; flame synthesis; nanoparticles

1. Introduction

Laser induced breakdown spectroscopy (LIBS) has been applied extensively to solids, liquids, gases, and aerosols in various environments [1–4]. LIBS has become a very popular analytical method due to its unique features such as no (or minimal) sample preparation, applicability to almost any type of sample in almost any environment, capability for *in-situ* measurements, and speed of analysis. LIBS analysis on aerosols have been employed in many conditions, such as coal gasification systems [5], ambient environments [6], experimentally controlled conditions [7,8], as well as single particles [9]. There have been efforts at gaining better understanding and extending the capability of LIBS on aerosols. Hybl et al. [10] discriminated biological agents from natural background aerosols based on different ratios of the atomic lines. Diwakar et al. [11,12] developed a near real-time measurement of elemental

compositions of aerosols of 30-900nm size at low concentrations by collecting particles onto a flat-tip microneedle electrode and then performing LIBS on the needle tip. Thärnhage et al. [13] aided LIBS with a trigger system such that the laser was fired only when a particle was expected in the focal zone, thus significantly increasing the hit rate for detection and classification of micrometer-sized single particles in real-time. Fortes et al. [14] combined optical catapulting (OC) and optical trapping (OT) with LIBS, permitting separation and manipulation of particles in a heterogeneous mixture, with subsequent analysis of the isolated particle of interest by changing the condition of optical trapping.

In our previous work [15], a novel low-intensity phase-selective LIBS method for nanoparticle detection during flame synthesis was developed. We demonstrated that unlike the conventional LIBS process for aerosols referenced above, the laser fluence is appropriately low so that only a nanoplasma is created around the nanoparticle with no gas-phase breakdown or macroscopically-observable plasma. Moreover, the breakdown occurs only when nanoparticles are present, allowing distinguishing of the elements from the solid particle phase. Thus, this technique is particularly helpful in understanding the gas-to-particle transition process. This technique has been further developed to achieve two-dimensional imaging of the gas-to-particle transition [16] and to measure the volume fractions of metal-oxide nanoparticles in a flow field [17]. The absorption-ablation-excitation mechanism in laser-cluster interactions of the low intensity LIBS process has been scrutinized by comparing Rayleigh scattering versus atomic emission of aerosol clusters in this regime [18].

In the current work, the effect of excitation wavelength is investigated using the third harmonic of the Nd:YAG laser in low-intensity phase-selective LIBS instead of the second harmonic as done in previous research. Interestingly, LIBS with subsequent resonant excitation

is observed. With low-intensity excitation (~30 mJ/pulse or 24 J/cm^2), only the titanium in the particle phase is selectively broken down, and the induced emission from the subsequent resonant excitation is markedly stronger than other emissions, demonstrating the capability to achieve a very low limit of detection for element(s) of interest from the nanoparticle phase.

2. Experimental setup

A stagnation swirl flame setup is utilized to synthesize TiO_2 nanoparticles, as shown in Fig. 1. The details of the setup can be found in Refs. [15,19]. In brief, the burner consists of an 18-mm diameter stainless-steel nozzle with an internal swirler, and a stagnation substrate (temperature controlled) is situated 19-mm downstream. Premixed CH_4, O_2 and N_2 flow into the burner, supporting a premixed flame, while a portion of the N_2 (2 L/min) runs through a bubbler containing TTIP precursor (titanium tetraisopropoxide) and carries the precursor to the flame. TiO_2 nanoparticles ~10 nm in size are formed for the given conditions.

The setup for the laser-based diagnostics is shown in Fig. 2. An injection-seeded Nd:YAG laser, that can run at second (532nm) or third (355nm) harmonic modes, serves as the excitation source. The output laser beam is focused by a 500-mm focal-length plano-convex fused silica lens to the region of interest in the nano-aerosol. The collection optics consist of two 400 mm focal-length achromats, an image rotator, and reflection mirrors. The emissions are collected at 90° into a triple spectrometer (Princeton Instruments TriVista), which is composed of two 0.5m spectrometers with 1800 groove/mm holographic grating and one 0.75m spectrometer with 1800 groove/mm holographic grating. An ICCD camera (Princeton Instruments PIMAX 3) detects the signal with selected delay and gate timing to minimize background interference and to study the temporal evolution of the process. A photomultiplier

tube (PMT, Hamamatsu R928), connected to the spectrometer at another port, with signals captured by a digital oscilloscope (Agilent Infiniium 54845A oscilloscope, 1.5 GHz sampling rate), further assesses the temporal evolution of the emissions at selected wavelengths. The typical slit width is set to 50-200 μm to minimize instrumental broadening and to obtain appropriate spatial and spectral resolutions.

3. Results and discussions

In order to achieve high stray light rejection and better spectral resolution, the triple spectrometer is first run in subtractive mode, where the first two stages work as a band pass filter and the third stage works as the main spectrometer. The entrance slit is set to 200 μm. The emission spectra from 532 nm and 355 nm laser excitation are shown in Fig.3. The laser power is 30 mJ/pulse for both cases and the signal collection time is 150 seconds.

For 532 nm excitation, the results are consistent with our previous work [15], where strong emissions at 498.173 nm, 499.107 nm, 499.950 nm, 500.721 nm, and 501.428 nm corresponding to Ti (I) atomic emission lines [20] from the nanoparticle-induced nanoplasmas are observed. However, for 355 nm excitation, a new high intensity emission at 497.534 nm appears. As will be discussed, this line likely corresponds to the Ti (I) atomic line produced by the transition from upper state $3d^3(^2D2)4p$ with term $w^1F°$ to lower state $3d^3(^2D2)4s$ with term b^1D. The line strength can be calculated from the expression [1]:

$$I = \frac{h\nu A_{ij} N_0 g}{4\pi Z} \exp(-\frac{E_j}{kT}) \quad (1)$$

where I is the emission intensity (W/sr); h is the Planck's constant; ν is the frequency; and A_{ij} is the transition probability (with Einstein A coefficient) from the upper state j to the lower state i

with energy difference of hv; N is the absolute number density of the atoms at upper state j; N_0 is the total number of atoms; Z is partition function, usually taken as the statistical weight of the ground state; E_j is the energy of the upper state; g is the statistical weight of energy state j; k is the Boltzmann's constant; and T is the electron temperature.

Based on the data from the National Institute of Standards and Technology (NIST) [20] and Wiese [21], and assuming an LTE (local thermodynamic equilibrium) plasma temperature of 10,000 K , the emission intensity at 497.534 nm should be less than 10% of the emission intensity at 498.173 nm. However, the experimentally measured emission intensity at 497.534 nm is about 5 times greater than that at 498.173 nm, indicating a mechanism beyond traditional LIBS or previously-studied PS LIBS.

To confirm that the 497.534nm line is from Ti atomic emission, rather than from intermediate species in the combustion and decomposition processes during flame synthesis, aerosolized Ti particles are examined. Ti particles are generated using the spark generator as given in the work by Byeon et al. [22]. Two titanium rods serve as electrodes, and 3kV are applied to the rods in an argon atmosphere, producing sparks/particles. Using focused excitation at '355nm,' strong emission at 497.534 nm is reproduced, confirming that the emission is indeed from atomic titanium.

As mentioned above, the 497.534 nm emission likely corresponds to the Ti (I) atomic line produced by the transition from upper state $3d^3(^2D2)4p$ with term $w^1F°$ to lower state $3d^3(^2D2)4s$ with term b^1D. The '355 nm' laser line is actually measured to be 354.71 nm, equivalent to one-third of the fundamental wavelength of the Nd:YAG laser at 1064.13 nm, which is consistent with the value from the literature [23]. Coincidentally, this laser line matches the Ti (I) absorption line at 354.703nm, with the upper state of this line being exactly the upper state of the

497.534 nm transition line, such that the electrons can be excited to the $3d^3(^2D2)4p$ upper state with term $w^1F°$. Besides the direct emission from the $w^1F°$ state, there can also be some internal transitions to other states, as the 480.541 nm emission (upper state $s^3D°$, with energy slightly lower than from the $w^1F°$ state) is also observed with high intensity.

There are several relevant mechanisms for describing this phenomenon, namely LIBS-LIF (laser induced fluorescence), RELIBS (resonant enhanced laser induced breakdown spectroscopy), and RLIBS (resonant laser induced breakdown spectroscopy). For LIBS-LIF, one laser pulse creates the plasma and another pulse excites selected states to produce fluorescence [24–27]. Two laser pulses, usually two lasers, are employed, which may result in system complexity. For RELIBS, one pulse performs the ablation and another pulse resonantly excites atoms, along with rekindling the plasma. A delay time of 30 ns or more relative to the second pulse is needed for signal collection [28,29]. For the RLIBS technique [30–34], which is a combination of resonant laser ablation (RLA) [35–38] and optical emission detection, only one laser pulse of selected wavelength is employed to create the plasma and also excite the electrons resonantly. In the RLIBS process, the first-come photons ablate the sample and then the other photons resonantly excite and ionize the vapor [39]. There are also some enhanced desorption for the ablation process [40], exothermic collision for vapor heating and reaching local thermodynamic equilibrium (LTE) [41], and transition of the energy from excited species to other components [31]. Based on the energy levels and the description of these three mechanisms, our observed phenomenon is most related to the RLIBS mechanism, with the 354.71 nm laser ablating the samples and then resonantly exciting the electrons of Ti atoms from a^1G sate to $w^1F°$ state. The excited electrons then undergo radiation processes, transitions, and exothermic collisions. It is worth noting that the a^1G state is not the ground state of Ti, and thus

the number of electrons in this state is not very large compared to that in the low-energy states, which means that the signal can be enhanced upon strategically selecting the excitation laser line.

RLIBS and RLA have been applied to major and trace element detections, manifesting part-per-billion sensitivity [30,37,38,42] and potential for quantitative measurements [33]. Some modeling work has been done to better understand the process [43]. However, for all the literature found, the RLIBS and RLA have been done with solid bulk samples or pure gas vapor. The work presents the first study of the RLIBS effect in nanoparticle aerosols. More importantly, combining of resonant ablation and low-intensity phase-selective LIBS will create some new features. Resonant ablation process is shown to be capable of selectively ionizing different target analyte from the same composite sample [42,44]. Combined with the low-intensity phase-selective LIBS on nanoparticles, it is possible to perform phase-selective and analyte-selective LIBS with low detection limit.

To demonstrate phase-selectivity, emission intensities along the centerline axis of the synthesis flow from 532 nm and 355 nm laser excitations are shown in Fig. 4. The 'total' intensities are calculated by integrating the emission from 497 nm to 502 nm. The emission intensities both show a quick increase at 5-12 mm downstream from burner exit, where the flame region is located, indicating phase change and particle growth. Nonetheless, differences exist for these two excitation wavelengths. At 2 mm downstream from burner exit (before particle growth), there is no emission around 500nm for 532nm excitation, while there is for 355 nm excitation, albeit with low intensity. Since in this low-swirl flame burner the gases and precursor are pre-mixed prior to the burner exit, the TTIP precursor encounters O_2, and there will be some reaction in the gas phase at ~ 100℃ to form some TiO_2 clusters at the burner exit, eventually producing TiO_2 particles at longer residence times [45,46]. These clusters can somehow absorb

the 355 nm laser light and be excited and broken down, while the 532 nm laser light cannot be absorbed much, due to different absorption efficiencies for the different wavelengths [47,48]. This dissimilar detection threshold for particle size may be further developed to be a quantitative method for size characterization.

To further investigate the characteristics of phase-selective LIBS with resonant 355 excitation on nanoparticles, the emission intensity change with laser intensity is studied, as shown in Fig. 5. The inset compares the emission intensity change at 532 nm laser excitation. For both cases, the measured location and precursor concentration are set to 14 mm downstream from the burner exit and 116 ppm respectively. The particle size is ~10 nm [15]. With 355 nm excitation, the laser power increases from 0.5 mJ/pulse to 35 mJ/pulse without gas-phase breakdown or visible plasma, which is observed at 40 mJ/pulse. The resonant emission at 497.534 nm can be detected and distinguished easily by the ICCD even at 0.5 mJ/pulse laser power, corresponding to a laser fluence of 0.4 J/cm^2, which is still above the breakdown threshold for most metals [49]. With 532 nm excitation, the LIBS emission intensity saturates at a laser power of 20 mJ/pulse, plateauing until gas breakdown at 70 mJ/pulse. Nevertheless, the emission intensities from 355 nm laser excitation exhibit no saturation, even up to gas-phase breakdown at 40 mJ/pulse. The saturation at 20 mJ/pulse with 532nm excitation corresponds to complete ablation of the particles. In contrast, PS-LIBS with 355 nm resonant excitation can continue to excite more electrons, with the upper state transitioning to other energy states, thus leading to continuous increasing of the 497.534 nm emission as well as other emissions.

The temporal evolution of the emissions at a laser power of 30 mJ/pulse is then investigated with gated ICCD camera and PMT. The gated ICCD camera records the emission spectrum at a gate width of 5ns with different delay times relative to the initial laser pulse. The

PMT obtains more detailed temporal evolution for emissions at a certain wavelength range. To obtain the temporal evolution using the ICCD with sufficient emission intensity, the camera is placed at the output of the first stage of the TriVista system; and the size of the entrance slit is set to 50 μm. While for the PMT setup, the PMT is placed at the output of the second state of the TriVista system, with the first and second stages working in the double subtractive mode as a fine band pass filter (with 40 μm intermediate slit size, corresponding to a width of 0.04 nm pass band).

The temporal evolution of the emission spectrum recorded by the ICCD camera from delay time 0 to 30 ns (the time when the laser pulse reaches its peak is set to 0) with 5 ns gate width is shown in Fig. 6. The curve at 0 ns delay time is the emission collected from 0 to 5 ns; the curve at 5 ns delay time is the emission collected from 5 ns to 10 ns, and so forth. Due to the property of the low-intensity phase-selective LIBS, the white noise is low even at 0 ns delay time. The 497.534 nm emission is fairly strong at 0 ns delay time and then decays with time until it vanishes at 25 ns delay time. However, for the other emissions, e.g. 498.173 nm, they increase from 0 to 10 ns delay time, and then decline gradually. They are still detectable at 30 ns delay time, disappearing at 35 ns delay time. The 497.534 nm emission decays faster than the 498.173 nm emission. As calculated above, for LTE, the 497.534 nm emission should be much weaker than for the 498.173 nm emission. The high emission intensity at 497.534 nm at the early stage is due to the selective excitation by the laser, which produces more electrons in the w^1F^0 state than that for the LTE condition.

Interestingly, at 0 ns delay time (peak of the laser excitation), the emission at 497.534 nm is composed of two peaks, and this is further investigated close to the laser time, i.e., from -10 ns delay to 0 ns delay, as shown in Fig. 7. At -10 ns delay time, there are two peaks straddling

497.534 nm, distinct from each other. At -5 ns delay time, the intensity of the emissions increases, and the two peaks get closer to each other. At 0 ns delay time, the two peaks get even closer, but are still distinguishable from each other. The two peaks are fitted with Lorentzian profile, and the center wavelength evolution is shown in the inset of Fig.7. The two peaks are 0.3 nm away from each other at -10 ns delay time, about 0.15 nm from 497.5 nm on both sides. Thereafter, they move towards 497.53 nm, and merge into one peak at 5 ns delay time. This splitting is attributed to influence of the magnetic field via the Zeeman effect. Magnetic field generated by laser-induced plasma has been observed since the early 70s [50] and is shown to be about coincident with the laser pulse [51]. The Zeeman effect has been employed to calculate the strengths of magnetic fields [51–53]. Based on the energy difference of the splitted peaks, the configuration of the electrons [20], and the formula given by Drake [54], the magnetic field is calculated to be 2.8 tesla, which may seem exceedingly large, but is actually consistent with the value given by McLean et al. [51] for laser power at this range.

Detailed temporal responses captured by PMT detector for different wavelengths are given in Fig. 8. The emissions around 497.53 nm are examined to show the detailed evolution of different wavelengths, i.e., from 497.35 nm to 497.70 nm at 0.05 nm intervals. The evolution of emission centered at 498.17 nm is also displayed for comparison. The pulse width (FWHM, full width at half maximum) of the laser is fitted to be 10 ns, and the time when the laser pulse reaches maximum peak is set to zero. The emissions around 497.53 nm increase rapidly when the laser pulse is present. However, the 498.17 nm emission rises slowly but lasts for a longer time. The sequence when the emissions reach their peaks is shown in Fig. 9. Relative to the laser pulse peak, the emissions around 497.53 nm climax about 3 to 6 ns later, while the 498.17 nm emission climaxes about 12 ns later. The emissions around 497.53 nm climax 6-9 ns prior to

the emission around 498.17 nm. The laser excites the electrons resonantly, leading to fast increase in emission at 497.53 nm. However, this emission is highly dependent on laser presence and decays as the laser pulse weakens. After the laser pulse ends at ~15 ns, the emissions around 497.53 nm last for another 15 ns, corresponding approximately to the transition decay time for the Ti (I) 497.534 nm line, which is on the order of $1/A_{ij} \approx 16$ ns based on the data given by Wiese [21].

Another interesting phenomenon is the dissimilarity observed for the emissions resulting from excitation laser with and without the injection seeder. For seeded laser excitation, as shown above, the 497.534 nm emission splits into two peaks with the onset of laser excitation. On the other hand, for unseeded laser excitation, the 497.534 nm emission does not split completely, but rather broadens. As shown in Fig. 10, the fitted FWHM is 0.18 nm at the beginning and then decays with time. The emission spectrum collected from -10 ns to -5 ns is shown in the inset. From 25 ns to 30 ns, there is no longer any emission, which is the same as for the seeded case. Moreover, the 480.54 nm emission is 4 times stronger for the excitation with unseeded versus seeded laser. The intensity change of the magnetic field produced and the line width change of the laser may also play a role. And further theoretic research is required regarding to this phenomenon.

4. Concluding Remarks

Novel low-intensity phase-selective laser induced breakdown spectroscopy (LIBS) with secondary resonant excitation from the same single laser pulse is employed in the *in-situ* study of flame synthesis of TiO_2 nanoparticles. Besides the phase-selectivity property of the low-intensity LIBS, the emission at 497.534 nm due to the secondary resonant excitation from the

same single laser pulse is much stronger than other/primary emissions. Due to the continuous resonant excitation of the atoms, the emissions show no plateauing as that with 532nm laser excitation. The 497.534nm emission is highly dependent on laser presence, climaxing prior to other emissions and decaying fast as the laser pulse weakens. The temporal evolution of the emissions also shows that the 497.534 nm emission split into two lines at the beginning, which is attributed to the magnetic field generated by the laser via the Zeeman effect.

The combination of phase-selective LIBS and resonant LIBS on nanoparticles measurement results in high intensity signal for the particle phase detection. The technique has the potential to make elemental measurements of nanoparticles at very-low detection limits, and make phase-selective analyte-selective measurements. With short focal-length lenses, the laser power can be lowered significantly while still maintaining strong signal. This can even be utilized with micro-LIBS technique [55–57] to improve the limit of detection. Besides the resonant LIBS process, there is also possibility to create lasing. Mirrorless lasing has been performed in air [58] and metal vapors [59], and lasing with titanium vapor at different wavelength are investigated [60–63]. With backward lasing, the remote detection with high signal intensity can be realized. This is the subject of on-going work.

Acknowledgements

This work was supported by the Army Research Office through grants W911NF-08-1-0417, W911NF-09-1-0138, and W911NF-10-1-0018. Special thanks are due to Ms. Aditi Kulkarni at Rutgers for assistance with flame synthesis and to Prof. Jeong Hoon Byeon at Yeungnam University, South Korea, for help with inert spark synthesis.

References

1. D. A. Cremers and L. J. Radziemski, *Handbook of Laser-Induced Breakdown Spectroscopy* (John Wiley & Sons, 2006).
2. A. W. Miziolek, Palleschi, and I. Schechter, *Laser-Induced Breakdown Spectroscopy (LIBS) Fundamentals and Applications* (Cambridge University Press, 2006).
3. D. W. Hahn and N. Omenetto, "Laser-induced breakdown spectroscopy (LIBS), part I: review of basic diagnostics and plasma–particle interactions: still-challenging issues within the analytical plasma community," Applied spectroscopy **64**, 335A–366A (2010).
4. D. W. Hahn and N. Omenetto, "Laser-Induced Breakdown Spectroscopy (LIBS), Part II: Review of Instrumental and Methodological Approaches to Material Analysis and Applications to Different Fields," Applied Spectroscopy **66**, 347–419 (2012).
5. L. J. Radziemski, T. R. Loree, D. A. Cremers, and N. M. Hoffman, "Time-resolved laser-induced breakdown spectrometry of aerosols," Anal. Chem. **55**, 1246–1252 (1983).
6. J. E. Carranza, B. T. Fisher, G. D. Yoder, and D. W. Hahn, "On-line analysis of ambient air aerosols using laser-induced breakdown spectroscopy," Spectrochimica Acta Part B: Atomic Spectroscopy **56**, 851–864 (2001).
7. R. G. Pinnick, P. Chylek, M. Jarzembski, E. Creegan, V. Srivastava, G. Fernandez, J. D. Pendleton, and A. Biswas, "Aerosol-induced laser breakdown thresholds: wavelength dependence," Applied optics **27**, 987–996 (1988).
8. D. W. Hahn and M. M. Lunden, "Detection and Analysis of Aerosol Particles by Laser-Induced Breakdown Spectroscopy," Aerosol Science and Technology **33**, 30–48 (2000).
9. D. W. Hahn, "Laser-induced breakdown spectroscopy for sizing and elemental analysis of discrete aerosol particles," Applied physics letters **72**, 2960–2962 (1998).
10. J. D. Hybl, G. A. Lithgow, and S. G. Buckley, "Laser-Induced Breakdown Spectroscopy Detection and Classification of Biological Aerosols," Applied Spectroscopy **57**, 1207–1215 (2003).
11. P. Diwakar, P. Kulkarni, and M. E. Birch, "New Approach for Near-Real-Time Measurement of Elemental Composition of Aerosol Using Laser-Induced Breakdown Spectroscopy," Aerosol Science and Technology **46**, 316–332 (2012).
12. P. K. Diwakar, K. H. Loper, A.-M. Matiaske, and D. W. Hahn, "Laser-induced breakdown spectroscopy for analysis of micro and nanoparticles," J. Anal. At. Spectrom. **27**, 1110–1119 (2012).
13. T. Tjärnhage, P.-Å. Gradmark, A. Larsson, A. Mohammed, L. Landström, E. Sagerfors, P. Jonsson, F. Kullander, and M. Andersson, "Development of a laser-induced breakdown spectroscopy instrument for detection and classification of single-particle aerosols in real-time," Optics Communications **296**, 106–108 (2013).
14. F. J. Fortes, A. Fernández-Bravo, and J. Javier Laserna, "Chemical characterization of single micro- and nano-particles by optical catapulting–optical trapping–laser-induced breakdown spectroscopy," Spectrochimica Acta Part B: Atomic Spectroscopy **100**, 78–85 (2014).
15. Y. Zhang, G. Xiong, S. Li, Z. Dong, S. G. Buckley, and S. D. Tse, "Novel low-intensity phase-selective laser-induced breakdown spectroscopy of TiO2 nanoparticle aerosols during flame synthesis," Combustion and Flame **160**, 725–733 (2013).
16. Y. Zhang, S. Li, Y. Ren, Q. Yao, and C. K. Law, "Two-dimensional imaging of gas-to-particle transition in flames by laser-induced nanoplasmas," Applied Physics Letters **104**, 023115 (2014).
17. Y. Zhang, S. Li, Y. Ren, Q. Yao, and S. D. Tse, "A new diagnostic for volume fraction measurement of metal-oxide nanoparticles in flames using phase-selective laser-induced breakdown spectroscopy," Proceedings of the Combustion Institute (n.d.).

18. Y. Ren, S. Li, Y. Zhang, S. D. Tse, and M. B. Long, "Absorption-Ablation-Excitation Mechanism of Laser-Cluster Interactions in a Nanoaerosol System," Phys. Rev. Lett. **114**, 093401 (2015).
19. J. Wang, S. Li, W. Yan, S. D. Tse, and Q. Yao, "Synthesis of TiO2 nanoparticles by premixed stagnation swirl flames," Proceedings of the Combustion Institute **33**, 1925–1932 (2011).
20. "NIST ASD Output: Lines," http://physics.nist.gov/cgi-bin/ASD/lines1.pl.
21. W. L. Wiese, "Atomic Transition Probabilities for Scandium and Titanium," J. Phys. Chem. Ref. Data **4**, (1975).
22. J. H. Byeon, J. H. Park, and J. Hwang, "Spark generation of monometallic and bimetallic aerosol nanoparticles," Journal of Aerosol Science **39**, 888–896 (2008).
23. J. Lu, M. Prabhu, K. Ueda, H. Yagi, T. Yanagitani, A. Kudryashov, and A. A. Kaminskii, "Potential of ceramic YAG lasers," LASER PHYSICS-LAWRENCE- **11**, 1053–1057 (2001).
24. S. L. Lui, Y. Godwal, M. T. Taschuk, Y. Y. Tsui, and R. Fedosejevs, "Detection of lead in water using laser-induced breakdown spectroscopy and laser-induced fluorescence," Analytical chemistry **80**, 1995–2000 (2008).
25. H. Loudyi, K. Rifaï, S. Laville, F. Vidal, M. Chaker, and M. Sabsabi, "Improving laser-induced breakdown spectroscopy (LIBS) performance for iron and lead determination in aqueous solutions with laser-induced fluorescence (LIF)," Journal of Analytical Atomic Spectrometry **24**, 1421 (2009).
26. F. Hilbk-Kortenbruck, R. Noll, P. Wintjens, H. Falk, and C. Becker, "Analysis of heavy metals in soils using laser-induced breakdown spectrometry combined with laser-induced fluorescence," Spectrochimica Acta Part B: Atomic Spectroscopy **56**, 933–945 (2001).
27. H. H. Telle, D. C. S. Beddows, G. W. Morris, and O. Samek, "Sensitive and selective spectrochemical analysis of metallic samples: the combination of laser-induced breakdown spectroscopy and laser-induced fluorescence spectroscopy," Spectrochimica Acta Part B: Atomic Spectroscopy **56**, 947–960 (2001).
28. S. L. Lui and N. h. Cheung, "Minimally destructive analysis of aluminum alloys by resonance-enhanced laser-induced plasma spectroscopy," Analytical Chemistry **77**, 2617–2623 (2005).
29. C. Goueguel, S. Laville, F. Vidal, M. Sabsabi, and M. Chaker, "Investigation of resonance-enhanced laser-induced breakdown spectroscopy for analysis of aluminium alloys," Journal of Analytical Atomic Spectrometry **25**, 635 (2010).
30. C. Goueguel, S. Laville, F. Vidal, M. Chaker, and M. Sabsabi, "Resonant laser-induced breakdown spectroscopy for analysis of lead traces in copper alloys," J. Anal. At. Spectrom. **26**, 2452–2460 (2011).
31. K. Rifai, F. Vidal, M. Chaker, and M. Sabsabi, "Resonant laser-induced breakdown spectroscopy (RLIBS) analysis of traces through selective excitation of aluminum in aluminum alloys," Journal of Analytical Atomic Spectrometry **28**, 388 (2013).
32. D. Cleveland, P. Stchur, and R. G. Michel, "Effect of background gas, sample angle and laser polarization on the enhancement effect of resonant laser ablation," Journal of Analytical Atomic Spectrometry **22**, 745 (2007).
33. D. Cleveland and R. G. Michel, "Quantitative analysis by resonant laser ablation with optical emission detection: Resonant laser-induced breakdown spectroscopy," Microchemical Journal **95**, 120–123 (2010).
34. F. J. Fortes, J. Moros, P. Lucena, L. M. Cabalín, and J. J. Laserna, "Laser-Induced Breakdown Spectroscopy," Anal. Chem. **85**, 640–669 (2013).
35. T. B. Lucatorto and T. J. McIlrath, "Efficient Laser Production of a Na+ Ground-State Plasma Column: Absorption Spectroscopy and Photoionization Measurement of Na+," Phys. Rev. Lett. **37**, 428–431 (1976).
36. C. G. Gill, T. M. Allen, J. E. Anderson, T. N. Taylor, P. B. Kelly, and N. S. Nogar, "Low-power resonant laser ablation of copper," Applied Optics **35**, 2069 (1996).

37. J. K. Gibson, "Resonant Laser Ablation of Lanthanides: Eu and Lu Resonances in the 450−470 nm Region," Anal. Chem. **69**, 111–117 (1997).
38. C. J. McLean, J. H. Marsh, A. P. Land, A. Clark, R. Jennings, K. W. D. Ledingham, P. T. McCombes, A. Marshall, R. P. Singhal, and M. Towrie, "Resonant laser ablation (RLA)," International Journal of Mass Spectrometry and Ion Processes **96**, R1–R7 (1990).
39. F. R. Verdun, G. Krier, and J. F. Muller, "Increased sensitivity in laser microprobe mass analysis by using resonant two-photon ionization processes," Analytical Chemistry **59**, 1383–1387 (1987).
40. D. Cleveland, P. Stchur, X. Hou, K. X. Yang, J. Zhou, and R. G. Michel, "Resonant laser ablation of metals detected by atomic emission in a microwave plasma and by inductively coupled plasma mass spectrometry," Applied spectroscopy **59**, 1427–1444 (2005).
41. C. Vadla, V. Horvatic, D. Veza, and K. Niemax, "Resonantly laser induced plasmas in gases: The role of energy pooling and exothermic collisions in plasma breakdown and heating," Spectrochimica Acta Part B: Atomic Spectroscopy **65**, 33–45 (2010).
42. G. C. Eiden, J. E. Anderson, and N. S. Nogar, "Resonant Laser Ablation: Semiquantitative Aspects and Threshold Effects," Microchemical Journal **50**, 289–300 (1994).
43. K. Watanabe and T. Iguchi, "Modeling of vaporization processes of resonant laser ablation," Appl Phys A **69**, S845–S848 (1999).
44. C. G. Gill, A. W. Garrett, P. H. Hemberger, and N. S. Nogar, "Resonant laser ablation as a selective metal ion source for gas-phase ion molecule reactions," J Am Soc Mass Spectrom **7**, 664–667 (1996).
45. D. M. Schleich and B. Walter, "Formation of titania nanoparticles by vapor phase reactions of titanium tetraisopropoxide in oxygen/ozone containing atmospheres," Nanostructured Materials **8**, 579–586 (1997).
46. S. Y. Kim, J. H. Yu, and J. S. Lee, "The characteristics of nanosized TiO2 powders synthesized by chemical vapor condensation," Nanostructured Materials **12**, 471–474 (1999).
47. H. Wu and L.-S. Wang, "Electronic structure of titanium oxide clusters: TiOy (y= 1-3) and (TiO2) n (n= 1-4)," Journal of Chemical Physics **107**, 8221–8228 (1997).
48. N. Serpone, D. Lawless, and R. Khairutdinov, "Size Effects on the Photophysical Properties of Colloidal Anatase TiO2 Particles: Size Quantization versus Direct Transitions in This Indirect Semiconductor?," J. Phys. Chem. **99**, 16646–16654 (1995).
49. L. M. Cabalin and J. J. Laserna, "Experimental determination of laser induced breakdown thresholds of metals under nanosecond Q-switched laser operation," Spectrochimica Acta Part B: Atomic Spectroscopy **53**, 723–730 (1998).
50. J. A. Stamper, K. Papadopoulos, R. N. Sudan, S. O. Dean, E. A. McLean, and J. M. Dawson, "Spontaneous magnetic fields in laser-produced plasmas," Physical Review Letters **26**, 1012–1015 (1971).
51. E. A. McLean, J. A. Stamper, C. K. Manka, H. R. Griem, D. W. Droemer, and B. H. Ripin, "Observation of magnetic fields in laser-produced plasma using the Zeeman effect," Physics of Fluids **27**, 1327 (1984).
52. H. Lin, J. R. Kuhn, and R. Coulter, "Coronal Magnetic Field Measurements," ApJ **613**, L177 (2004).
53. E. Stambulchik, K. Tsigutkin, and Y. Maron, "Spectroscopic Method for Measuring Plasma Magnetic Fields Having Arbitrary Distributions of Direction and Amplitude," Phys. Rev. Lett. **98**, 225001 (2007).
54. G.W.F. Drake, *Springer Handbook of Atomic, Molecular, and Optical Physics* (Springer, 2006).
55. M. Corsi, G. Cristoforetti, M. Giuffrida, M. Hidalgo, S. Legnaioli, L. Masotti, V. Palleschi, A. Salvetti, E. Tognoni, C. Vallebona, and A. Zanini, "Archaeometric Analysis of Ancient Copper Artefacts by Laser-Induced Breakdown Spectroscopy Technique," Microchimica Acta **152**, 105–111 (2005).

56. A. Giakoumaki, K. Melessanaki, and D. Anglos, "Laser-induced breakdown spectroscopy (LIBS) in archaeological science—applications and prospects," Analytical and Bioanalytical Chemistry **387**, 749–760 (2007).
57. D. Menut, P. Fichet, J.-L. Lacour, A. Rivoallan, and P. Mauchien, "Micro-laser-induced breakdown spectroscopy technique: a powerful method for performing quantitative surface mapping on conductive and nonconductive samples," Applied optics **42**, 6063–6071 (2003).
58. A. Dogariu, J. B. Michael, M. O. Scully, and R. B. Miles, "High-Gain Backward Lasing in Air," Science **331**, 442–445 (2011).
59. A. Sharma, N. D. Bhaskar, Y. Q. Lu, and W. Happer, "Continuous-wave mirrorless lasing in optically pumped atomic Cs and Rb vapors," Applied Physics Letters **39**, 209–211 (1981).
60. H. Ninomiya and K. Hirata, "Laser action of optically pumped atomic titanium vapor," Journal of Applied Physics **66**, 2219–2220 (1989).
61. H. Ninomiya and K. Hirata, "Visible laser action in N2-laser-pumped Ti vapor," Journal of Applied Physics **68**, 5378–5380 (1990).
62. K. Hirata, S. Yoshino, and H. Ninomiya, "Optically pumped titanium vapor laser at 551.4 nm," Journal of Applied Physics **67**, 45–48 (1990).
63. H. Ninomiya, K. Hirata, and S. Yoshino, "Optically pumped titanium vapor laser at 625.8 nm," Journal of Applied Physics **66**, 3961–3962 (1989).

Figures:

Figure Captions list:

Fig. 1. Schematic of the stagnation swirl flame setup with TEM of particles collected on substrate

Fig. 2. Schematic of the laser diagnostic system

Fig. 3. Emissions around 500 nm from 532 nm (a) and 355 nm (b) laser excitation

Fig. 4 Signal intensity along axis at 532 nm and 355 nm laser excitation

Fig. 5. Intensity change with laser power for 497.534 nm and other emissions, inset shows the intensity change with laser power at 532nm laser excitation.

Fig. 6. Temporal evolution of the emission spectrum from 0 to 30 ns delay time

Fig. 7 Temporal evolution of the emission spectrum from -10 to 0 ns delay time, the inset shows the center wavelength of peaks from -10 to 5 ns delay time

Fig 8. Temporal evolution of the emission for different wavelengths

Fig. 9. Relative time (to the laser peak) for the emissions to reach peak value

Fig. 10. Peak width of 497.534 nm emission excited with unseeded laser, the inset shows the spectrum collected from -10ns to -5 ns delay time

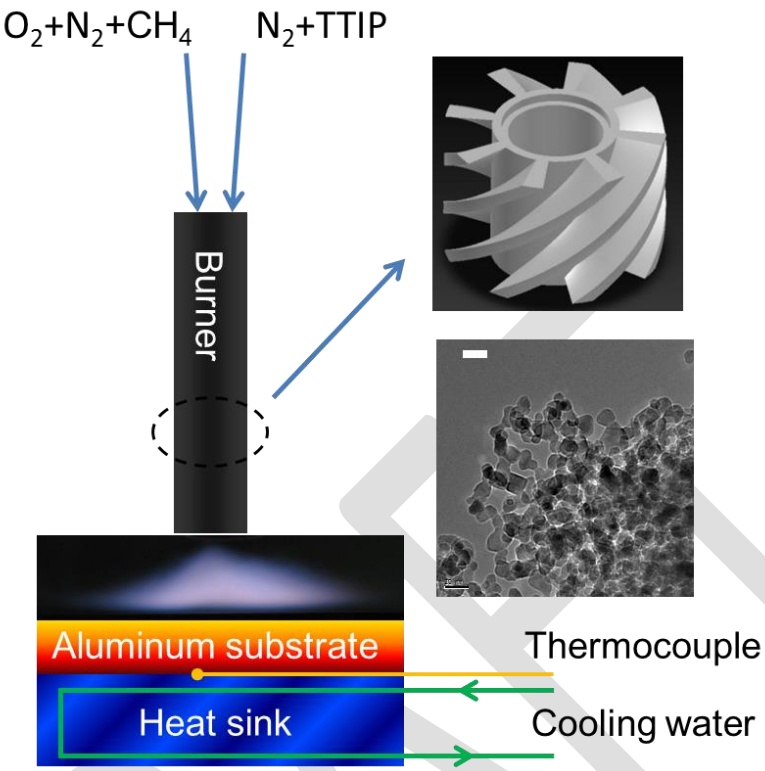

Fig. 1. Schematic of the stagnation swirl flame setup with TEM of particles collected on substrate, the scale bar is 20 nm, showing particle size of ~10nm

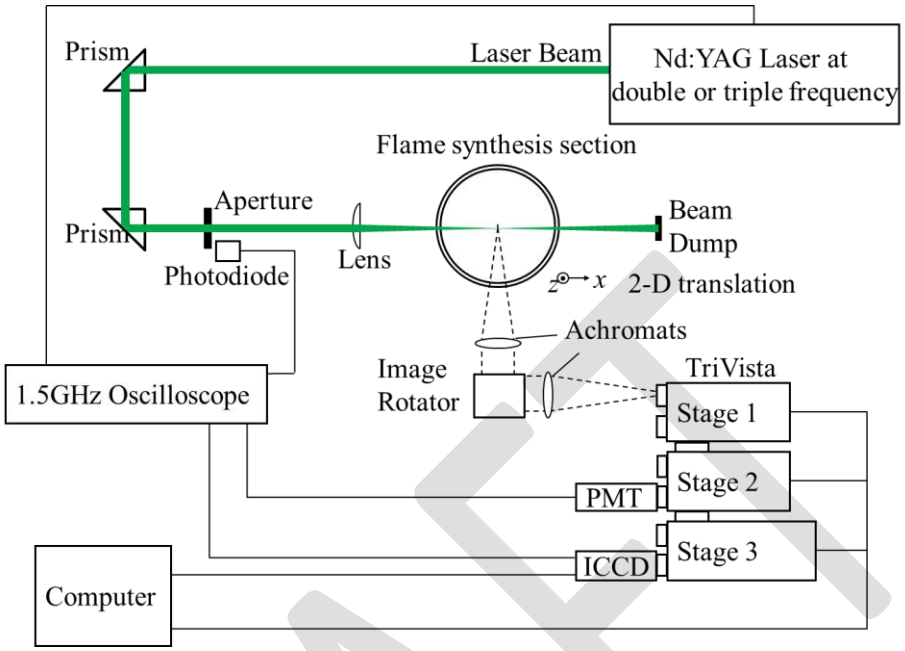

Fig. 2. Schematic of the laser diagnostic system

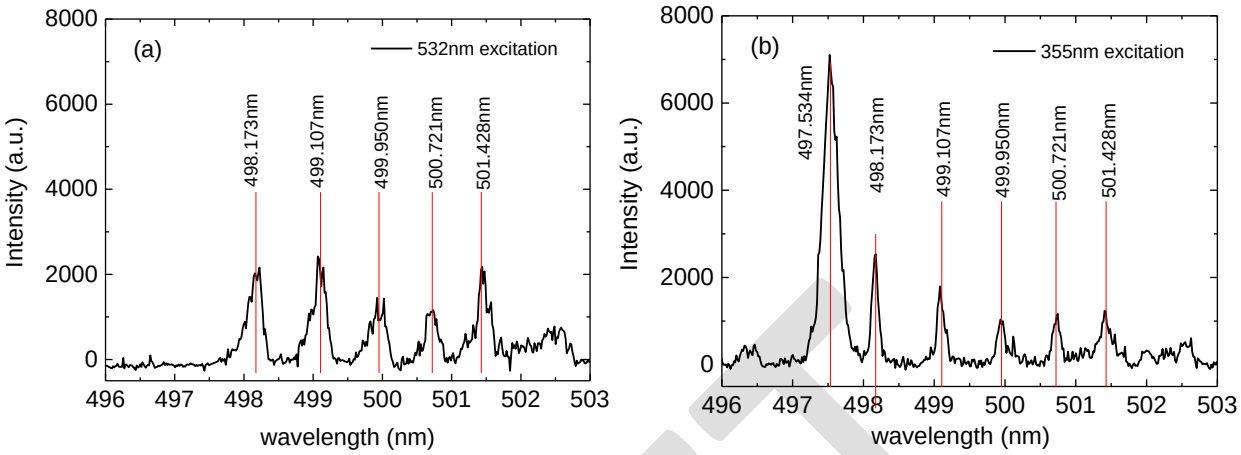

Fig. 3. Emissions around 500 nm from 532 nm (a) and 355 nm (b) laser excitation

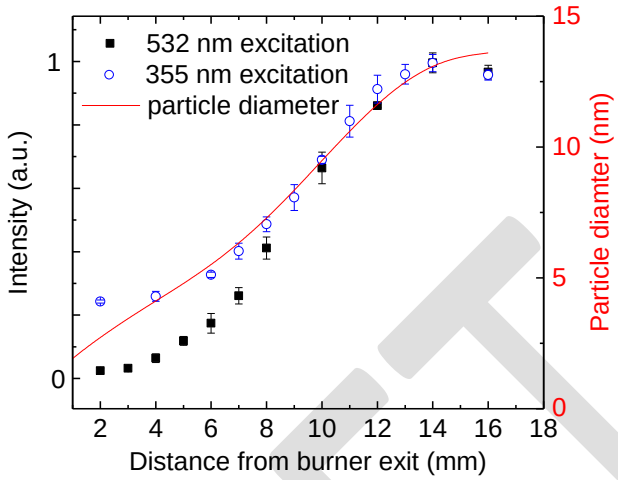

Fig. 4 Signal intensity along axis at 532 nm and 355 nm laser excitation

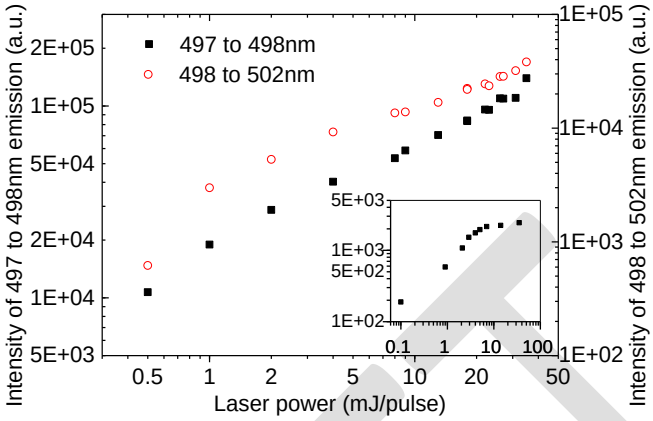

Fig. 5. Intensity change with laser power for 497.534 nm and other emissions, inset shows the intensity change with laser power at 532nm laser excitation.

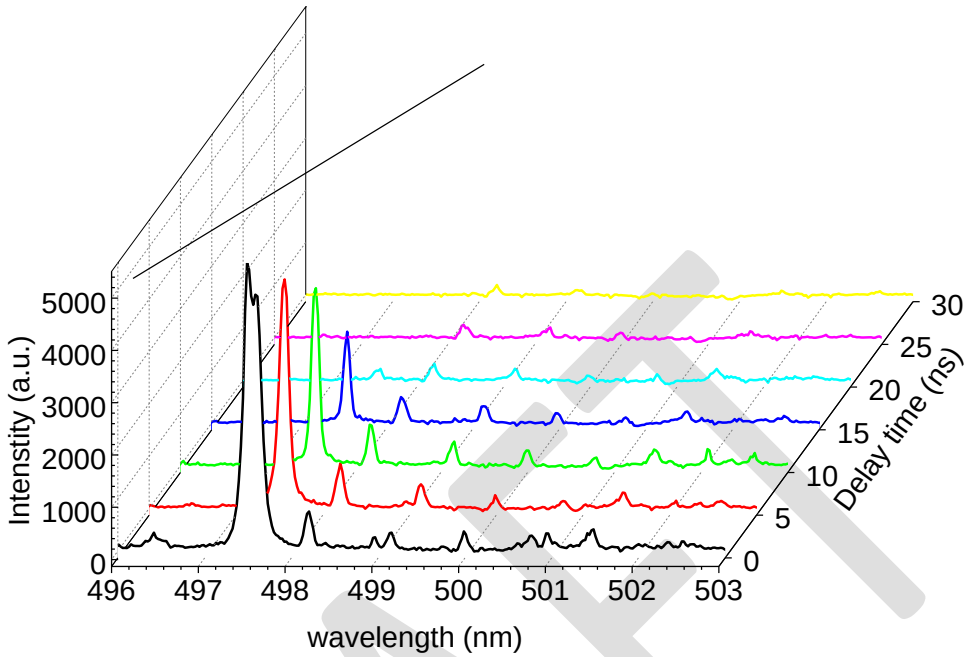

Fig. 6. Temporal evolution of the emission spectrum from 0 to 30 ns delay time

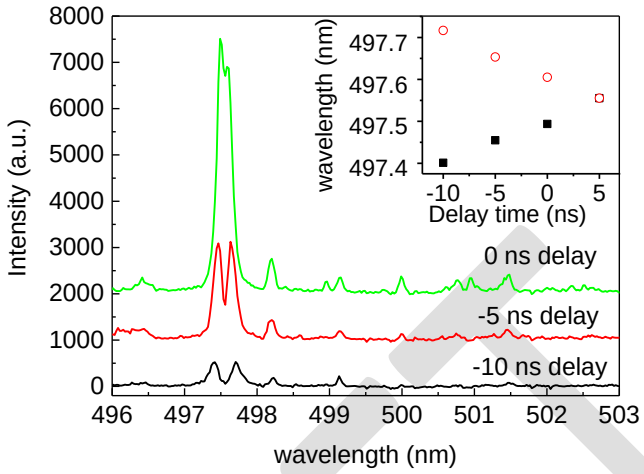

Fig. 7 Temporal evolution of the emission spectrum from -10 to 0 ns delay time, the inset shows the center wavelength of peaks from -10 to 5 ns delay time

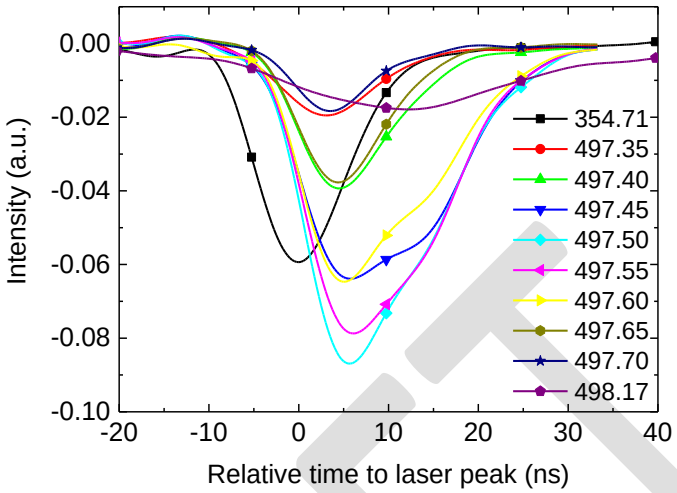

Fig 8. Temporal evolution of the emission for different wavelengths

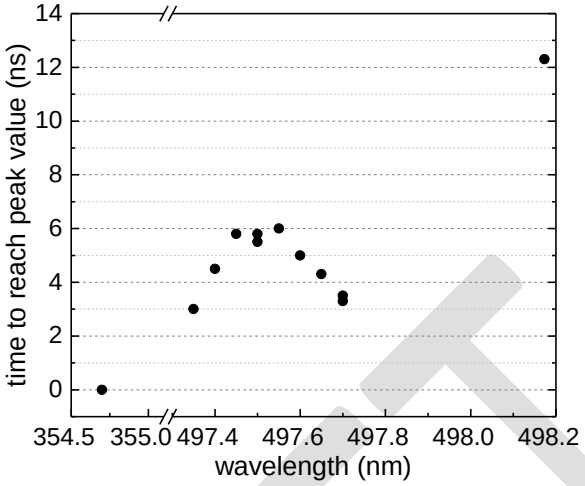

Fig. 9. Relative time (to the laser peak) for the emissions to reach peak value

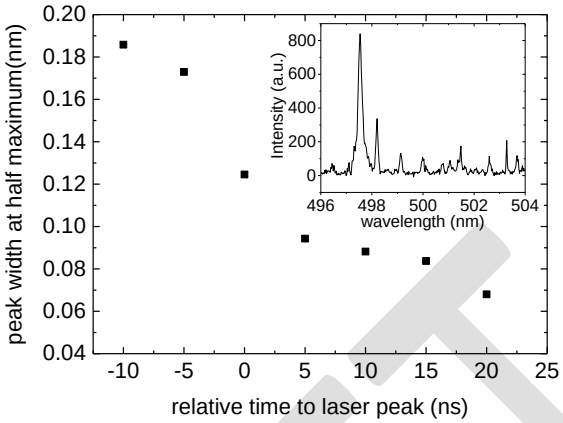

Fig. 10. Peak width of 497.534 nm emission excited with unseeded laser, the inset shows the spectrum collected from -10ns to -5 ns delay time

Combined Flame and Solution Synthesis of Tungsten-Oxide and Zinc/Tin-Oxide Nanoheterostructures

Zhizhong Dong[1], Di Huo[1,3], Bernard Kear[2], and Stephen D. Tse[1*]

[1]*Department of Mechanical and Aerospace Engineering, Rutgers University, USA*

[2]*Department of Materials Science and Engineering, Rutgers University, USA*

[3]*School of Materials and Metallurgy, Northeastern University, China*

** corresponding author. sdytse@rci.rutgers.edu*

Abstract

Several new kinds of heterostructures of $WO_{2.9}$ nanowires with ZnO/SnO_2 nanostructures have been synthesized via a combined flame and solution synthesis method. First, vertically well-aligned single-crystal tungsten-oxide nanowires are grown directly on a tungsten substrate via a flame synthesis method. Here, $WO_{2.9}$ nanowires are produced by the vapor-solid (VS) mechanism, with gas phase species (O_2, H_2O, CO_2, and H_2) and local gas phase temperature (1720K) specified at the substrate for desired growth, e.g. diameters of 20-50nm, lengths > 10μm, and coverage density of 10^9-$10^{10}cm^{-2}$. Then, various kinds of ZnO/SnO_2 nanostructures are grown on the $WO_{2.9}$ nanowires by adjusting the concentration ratio of Zn^{2+} and Sn^{2+} in an aqueous ethylenediamine solution. With $WO_{2.9}$ nanowires serving as the scaffold, sequential growth of hexagonal ZnO nanoplates, Zn_2SnO_4 nanocubes, and SnO_2 nanoparticles are attained for Zn^{2+}:Sn^{2+} ratios of 1:0, 10:1, and 1:10, respectively. High-resolution transmission electron microscopy (HRTEM) of the interfaces at the nanoheterojunctions show atomically abrupt interfaces for $ZnO/WO_{2.9}$ and $Zn_2SnO_4/WO_{2.9}$, despite lattice mismatches of >20%. The process demonstrated in this work might provide a rapid, readily scaled, and versatile synthesis route for development of functional nanoheterostructures.

Introduction

Heterostructured nanomaterials have attracted significant attention due to their unique physical and chemical properties, allowing them to be employed in novel electronic, photonic, and chemical sensor devices [1-4]. Various low dimensional nanostructures have been used as building blocks in multicomponent and complex nanostructures, such as core/shell nanowires [8], epitaxial heterostructured nanowires [2,3,5], and hierarchical heterostructures [6,7]. Avoidance of lattice mismatches between nano-scale materials with different lattice constants can provide promising high electronic performance, which usually cannot be obtained from their bulk counterparts [1,2]. Wu et al. [2] successfully fabricated NiSi/Si segmental nanowires with atomically sharp interface. A field-effect transistor (FET) device demonstrated the spatially and electronically well-defined interface between NiSi (growth direction of [221]) and Si (growth direction of [112]). Milliron et al. [3] grew epitaxially CdTe on the tip of CdS nanorods, which exhibited stacking-fault-free continuous growth of linear junctions despite large lattice mismatch (11%) between CdTe and CdS. Typically, multiple synthesis steps, e.g. involving solution-liquid-solid (SLS) [5, 6], solution-solid (SS) [24], vapor-liquid-solid (VLS), and vapor-solid (VS) [7] mechanisms, are utilized to produce heterostructured nanomaterials. Via the Bi-assisted SLS method, Ouyang et. al. [5] prepared CdS/CdSe nanorod heterojunctions with low stacking faults (<5%) regardless of the diameter difference between CdS (diameter of 15-80 nm) and CdSe (diameter of 20-130 nm). Using solution synthesis, Zhang et al. [6] produced hierarchical α-Fe_2O_3/SnO_2 heterostructures where SnO_2 nanorods were grown vertically on the surface of α-Fe_2O_3 nanotubes (diameter of 100-110 nm). The results indicated that lattice mismatch at the interface may lead to [101] growth of SnO_2 nanorods rather than the usual [001] direction. Tungsten-oxide based heterostructured nanomaterials have also been produced. Baek et al. [7]

fabricated hierarchical W/WO_3 heterojunctions, where W nanorods (diameters of 20-60 nm) were grown on the surface of WO_3 stems (diameters of 200-500 nm); the W/WO_3 heterojunctions displayed excellent field emitting properties with a turn-on field of 6.2 $V\mu m^{-1}$. Kim et al. [9] decorated WO_3 nanowhiskers (diameters of 80 nm - 1 μm) with CdS nanoparticles (diameters of 20-50 nm), which possessed enhanced photocatalytic efficiencies, using a two-step process involving thermal evaporation and chemical bath deposition. Other tungsten oxide related heterostructured nanomaterials include $SnO_2/W_{18}O_{49}$ hierarchical heterojunctions [10], TiO_2/WO_3 core/shell nanoparticles [11], and Pd/WO_3 heterojunctions [12]. Here, we report the epitaxial growth of ZnO nanostructures (produced by solution synthesis) on $WO_{2.9}$ nanowires (produced by flame synthesis). Specifically, hexagonal ZnO nanoplates, Zn_2SnO_4 nanocubes, and SnO_2 nanoparticles are grown on $WO_{2.9}$ nanowires, where the composition and morphology of the added nanostructures are controlled by the ratio of zinc to tin ions in the aqueous solution.

Experiment

A schematic of the experimental setup is given in Fig. 1. In the first step, a counter-flow diffusion flame synthesizes well-aligned tungsten-oxide nanowires directly on a tungsten substrate [19], as shown in Figure 1(a). The burner configuration consists of two convergent nozzles with a 19-mm exit diameter and 15-mm separation distance. Airflow as oxidizer is issued from the top burner, and nitrogen-diluted methane flow is issued from the bottom burner, establishing a flat flame in-between. Co-flowing nitrogen eliminates oxidizer entrainment into the flame, extinguishes the outer flame, and minimizes shear instabilities. For the relative concentrations of fuel and oxidizer used in our experiments, the flame is located on the oxidizer side of the stagnation surface. A tungsten substrate probe (0.8 mm) is inserted into the oxidizer side of the flow field (where the gas-phase temperature is 1720 K), and arrays of $WO_{2.9}$

nanowires grow from it. The synthesis method is robust in that the combustion process inherently provides for i) an elevated enthalpy source to evaporate metal substrate atoms, ii) the gas-phase chemical species e.g., oxidizer, water vapor, and hydrogen to produce the requisite oxide, and iii) a favorable temperature gradient for growth of the nanowires.

In the second step, solution synthesis is utilized to grow different compositions and morphologies of nanomaterials on the scaffold nanowires, as shown in Figure 1 (b), forming new heterojunctioned nanomaterials. Specifically, the substrate is placed into ethylenediamine ($C_2H_8N_2$) (97%, Fisher Scientific) solutions with different amounts of precursor compositions and concentrations, as shown in in Table 1, at 338.15 K for 2.5 hours under atmosphere pressure. For Case 1, the solution contains only zinc nitrate hexahydrate ($Zn(NO_3)_2{\cdot}6H_2O$) (98%, Fisher Scientific) as precursor, which provides the Zn ions to form the desired $ZnO/WO_{2.9}$ heterostructrured nanomaterials. From Cases 2-7, progressively more Sn ions comprise the aqueous solution, affecting the final composition of the as-produced nanostructures. For Case 8, the solution contains only tin chloride dehydrate ($SnCl_2{\cdot}2H_2O$) (98%, Fisher Scientific) as precursor, which provides only Sn ions to form the desired SnO_2/WOx heterostructured nanomaterials.

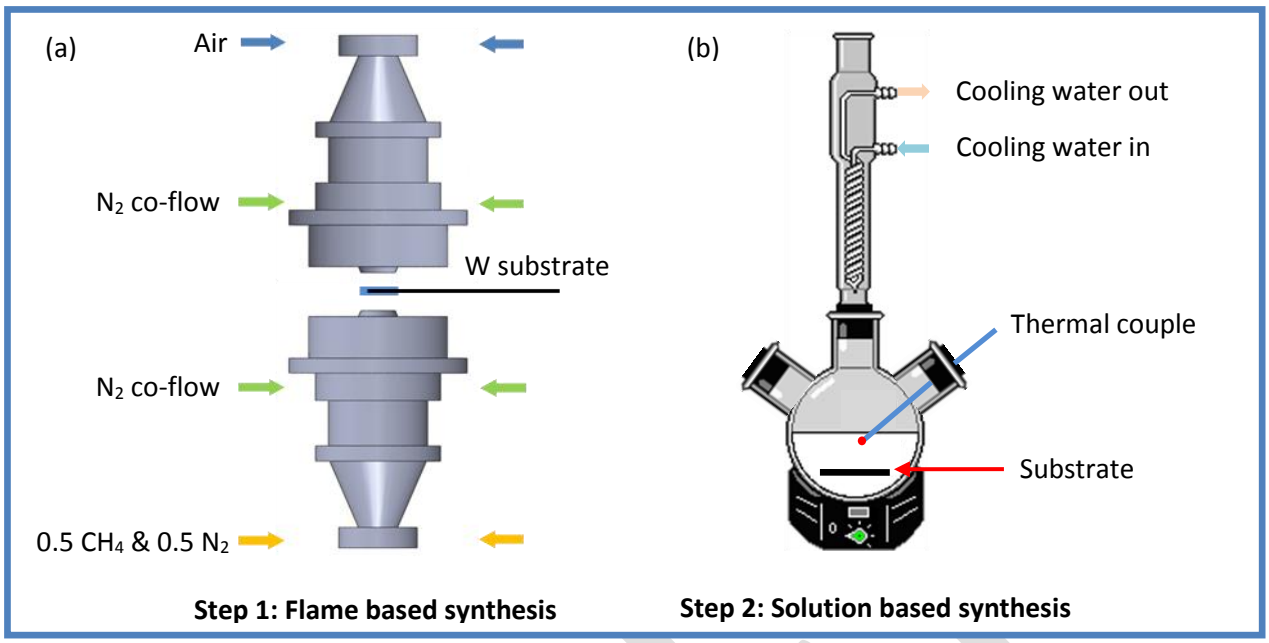

Figure 1. Schematic diagram of the experimental setup. (a) 1st step, the growth of WOx nanowires via flame synthesis method. (b) 2nd step, the growth of heterojunctions via solution synthesis method.

Table 1. Composition of solution for different cases.

Case number	Concentration (mol/L)		
	Ethylenediamine $C_2H_8N_2$	Zinc nitrate hexahydrate $Zn(NO_3)_2{\cdot}6H_2O$	Tin chloride dehydrate $SnCl_2{\cdot}2H_2O$
Case 1	0.005	0.005	0
Case 2	0.005	0.005	0.0005
Case 3	0.005	0.004	0.001
Case 4	0.005	0.003	0.002
Case 5	0.005	0.002	0.003
Case 6	0.005	0.001	0.004
Case 7	0.005	0.0005	0.005
Case 8	0.005	0	0.005

During the solution synthesis process, ethylenediamine (EDA) gradually decomposes around 338.15 K, continuously providing ammonia which then forms ammonium hydroxide and complex intermediates with zinc and tin ions [14]. The dehydration of these intermediates leads to the formation of the desired oxides, namely ZnO, Zn_2SnO_4, and SnO_2. The proposed reaction routes are [13-18]:

$$C_2H_8N_2 + 2H_2O \leftrightarrow 2NH_3 + C_2H_6O_2 \quad (1)$$

$$NH_3 + 2H_2O \leftrightarrow NH_4^+ + OH^- \quad (2)$$

$$2OH^- + Zn^{2+} \rightarrow ZnO(s) + H_2O \quad (3)$$

$$8OH^- + 2Zn^{2+} + Sn^{2+} \rightarrow Zn_2SnO_4(s) + 4H_2O \quad (4)$$

$$4OH^- + Sn^{2+} \rightarrow SnO_2(s) + 2H_2O \quad (5)$$

In the formation of ZnO, Equations (1, 2, 3) likely take place. OH^- can be generated through Equations (1, 2), followed by reaction with Zn^{2+}. After the dehydration of zinc related intermediates, the desired ZnO species can be produced, as shown in Equation (3). Similarly, Zn_2SnO_4 and SnO_2 can also be produced through Equations (1, 2, 4) and Equations (1, 2, 5), respectively.

The morphologies of as-produced samples are investigated using field emission scanning electron microscopy (FESEM). Elemental analysis is performed using energy dispersive X-ray spectroscopy (EDS) attached to the FESEM. Structural features of the samples are investigated using high resolution transmission electron microscopy (HRTEM), and chemical phase is determined using selected area electron diffraction (SAED).

Results and Discussion

Tungsten-oxide nanowire arrays

The FESEM images of tungsten-oxide nanowires are presented in Figure 2. The images show a high-density of nanowires growing directly from the surface of the tungsten substrate. The as-grown nanowires (Fig. 2(b)) have diameters of 20–50 nm, with lengths > 10 μm.

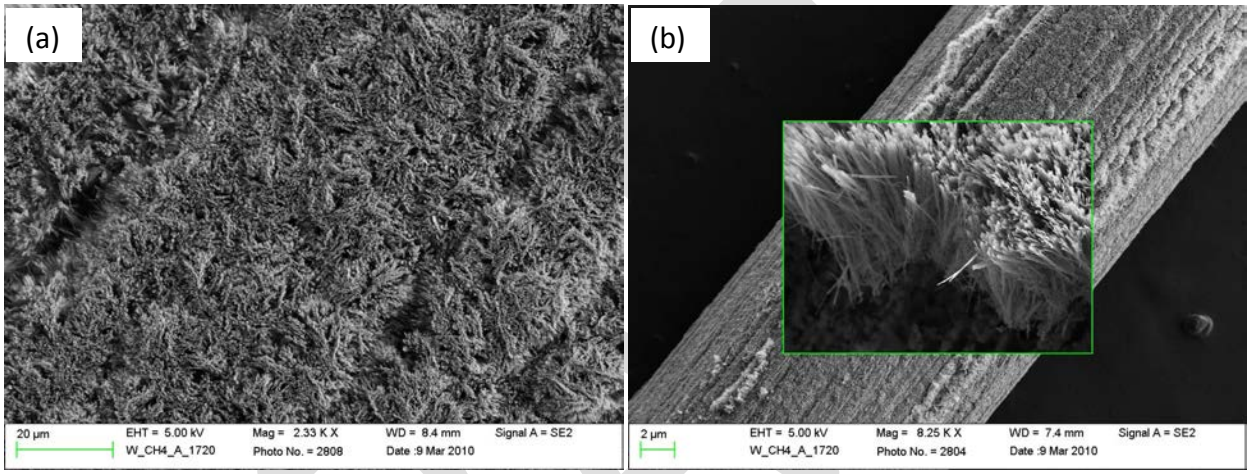

Figure 2. (a) Low magnification FESEM image of as-grown tungsten oxide nanowires showing high density of yield. (b) Typical FESEM image of as-grown tungsten oxide nanowires from a side view revealing the vertically aligned growth direction.

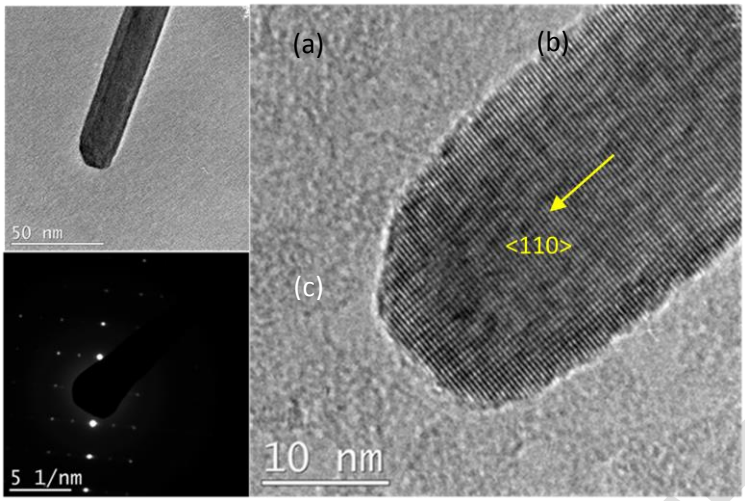

Figure 3. (a) Typical side-view low magnification TEM image of as-synthesized tungsten oxide nanowire. (b) HRTEM image of as-produced tungsten oxide nanowire. (c) Selected area electron diffraction (SAED) pattern of as-produced tungsten oxide nanowire.

Figure 3(a) presents a low-magnification TEM image of a single as-produced tungsten-oxide nanowire, revealing is well-defined shape and structure. Figure 3(b) shows an HRTEM image which indicates the dislocation-free and single-crystal nature of a nanowire. The growth direction is <110>; and the indexed SAED pattern gives three d-spacings of 3.755, 3.137, and 2.314 Å, which match well with the tetragonal phase (space group P4 / nmm) of $WO_{2.9}$ (PDF card NO. 18-1417). The d-spacings correspond to {110}, {101}, and {201}, respectively.

ZnO hexagonal nanoplates on the tips of WO_x nanowires (Case 1)

As shown in Fig. 4(a), abundant heterostructured nanomaterials are found on the surface of the tungsten substrate. Nearly all tips of WOx nanowires are capped with hexagonally-shaped ZnO

nanoplates, with no ZnO nanostructures found elsewhere. In Fig. 4(b), a high magnification FESEM image shows a side view of a heterojunction, which evinces epitaxial growth of ZnO on the tip of WOx. The diameter of the hexagonal ZnO nanoplate is ~200 nm, significantly larger than that of the supporting nanowire, and the thickness is ~60 nm. Here, the hexagonal shape of the ZnO nanoplate provides strong evidence for the <0001> growth direction of ZnO [21]. It is possible that the thickness of the ZnO nanostructures can be further increased by longer processing times.

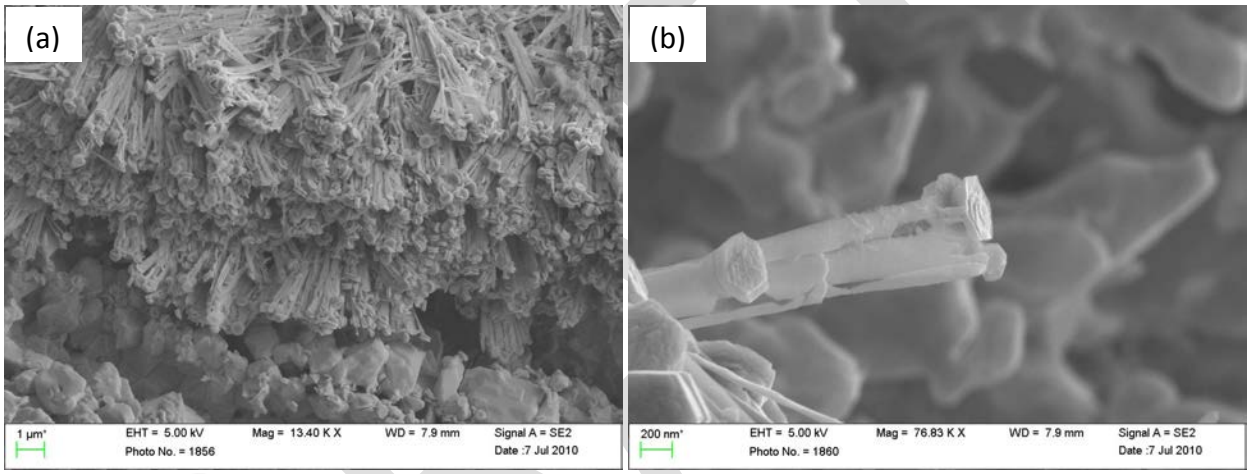

Figure 4. FESEM images of the as-produced ZnO/WOx heterojunctions. (a) Low magnification image showing abundance of as-grown heterostructures. (b) High magnification image showing the side view of a single heterostructure. The $WO_{2.9}$ nanowire is capped by a ZnO nanoplate which has the typical hexagonal structure. The edge of hexagon is ~200nm.

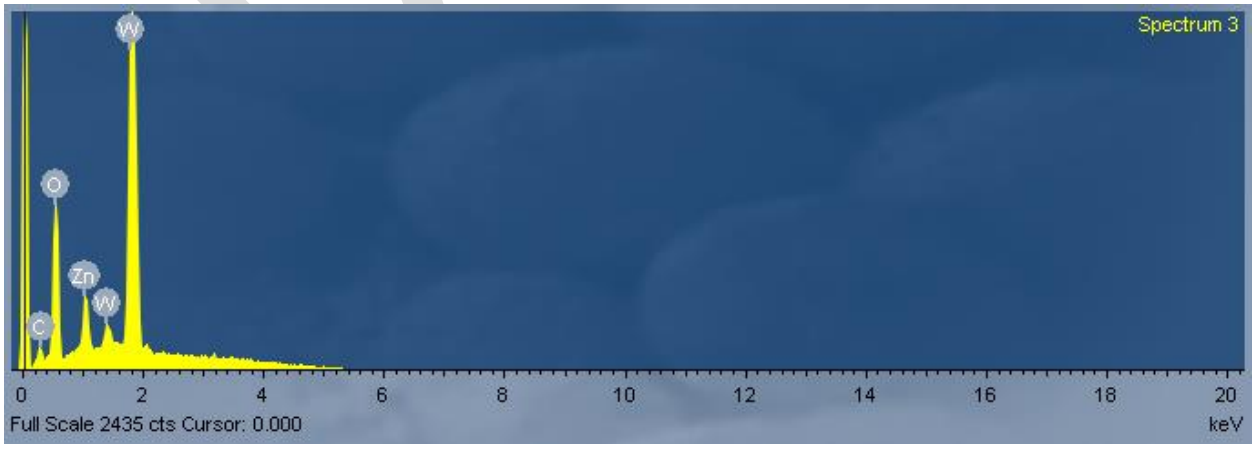

Figure 5. EDS spectrum of as-grown ZnO/WOx heterojunctions.

A typical EDS spectrum of as-prepared ZnO/WOx heterostructures in Fig. 5 corroborates the presence of elemental oxygen (O), zinc (Zn), and tungsten (W), along with a small amount of carbon (C), that is probably deposited on the surface of the WOx nanowires during synthesis [19] or from residue in the solution.

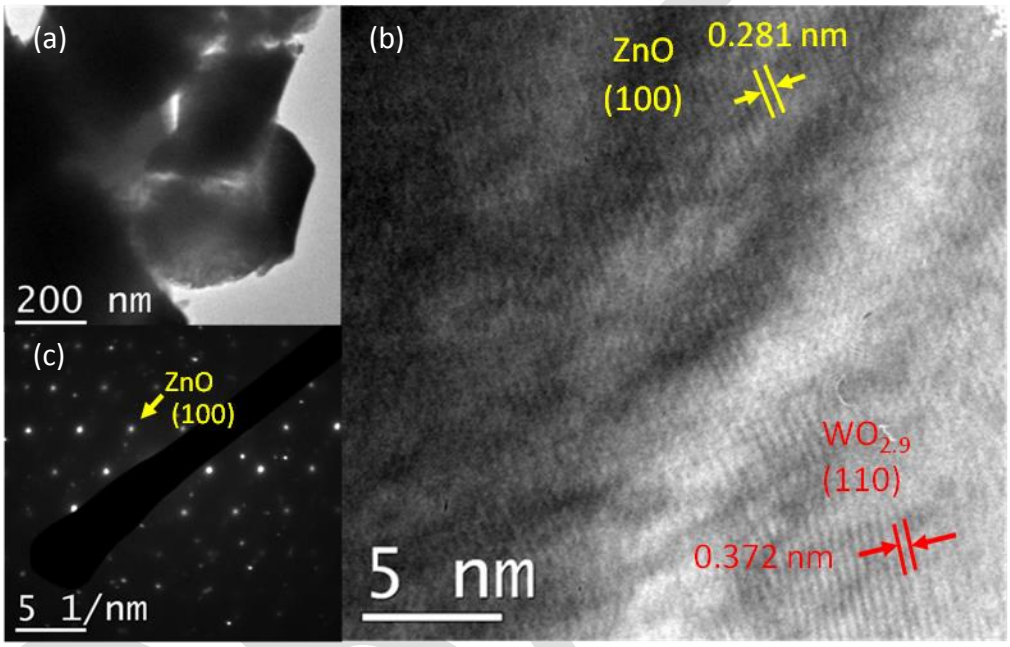

Figure 6. (a) Typical side-view low magnification TEM image of as-synthesized ZnO/$WO_{2.9}$ heterojunction. (b) HRTEM image of the ZnO/$WO_{2.9}$ heterojunction. (c) Selected area electron diffraction pattern (SAED) of ZnO/$WO_{2.9}$ heterojunction.

Figure 6(a) presents a low-magnification TEM micrograph of the ZnO/$WO_{2.9}$ heterojunction, confirming epitaxial growth of ZnO on WOx. Hou et al. [20] observed epitaxial growth of ZnO nanowires at the nodes of ZnO nanowalls, where such nodes are believed to be the most thermodynamically active nucleation sites. In this work, the tips of the tungsten oxide nanowires play the similar role as those nodes for the nucleation of ZnO nanostructures. Furthermore, the enlarged growth of the ZnO nanostructures in the radial direction is most likely promoted via the self-assembly [20,25] and solution-solid (SS) mechanisms [24], with no

catalysts involved as is typical for VLS [26] and SLS mechanisms [22]. Similar to the VS mechanisms for gas-phase synthesis [7], precursors containing zinc-related atoms, ions, and molecules in the solution diffuse to favorable nucleation sites and continuously promote the growth of the ZnO nanostructures under supersaturated conditions [22-26]. Finally, optimized energy compensation will be purchased under certain circumstance resulting to the as-synthesized heterojuncions [20,23,25].

Figure 6 (b) presents a HRTEM micrograph of the ZnO/$WO_{2.9}$ heterostructure. Due to the relatively large lattice mismatch of 22.8% between $WO_{2.9}$ (110) planes (lattice fringes of 0.372 nm) and ZnO (100) planes (lattice fringes of 0.281 nm), slight stacking faults can be observed at the interface region. Similar interface structures were found in CdS/CdSe heterojunctions with slight stacking faults (<5%), as reported by Ouyang et.al [5]. For very large lattice mismatches, high density defects between Zn (101) planes (lattice fringes of 0.21 nm) and ZnS (0001) planes (lattice fringes of 0.63 nm) were observed by Shen et al. [27]. Moreover, atomically sharp interfaces of heterojunctions have been successfully fabricated, such as for NiSi/Si [2], CdTe/CdS [3], and Ge/ZnS [27]. As found in the literature [1, 25], atomically abrupt interfaces can readily be obtained between two materials with matched lattice structures, e.g. as shown by Shen et.al [27]. However, it is also possible for two materials with lattice mismatches to form atomically abrupt interfaces or slight defect-containing interfaces under nanoscale, driven by self-assembly mechanisms [1,25]. As shown in Fig. 6(c), the indexed SAED pattern with d-spacing of 2.79 Å matches well with {100} planes of the hexagonal phase (space group P63mc) of ZnO (PDF card NO. 15-5780), further verifying the (100) plane of ZnO as measured from the HRTEM micrograph of Fig. 6(b).

Zn_2SnO_4 nanocubes on the tips of WOx nanowire (Cases 2-4)

Various spinels (space group Fd3m [30]) crystallizing in a cubic-shaped structure has been produced, such as $ZnFe_2O_4$ [28], $ZnAl_2O_4$ [29], and Zn_2SnO_4 [31-35]. Zinc stannate compounds are widely used for sensors [35], photocatalysts [33], solar cells [32], and anodes for Li-ion batteries [34]. In this work, tin chloride dihydrate (0.0005 M) is introduced into an aqueous ethylenediamine (0.005M) solution containing zinc nitrate hexahydrate (0.005 M) to produce the desired spinel compound of zinc stannate (ZTO, Zn_2SnO_4), corresponding to case 2 of Table 1. A top-view low-magnification FESEM image (Fig. 7(a)) shows an abundance of as-grown Zn_2SnO_4/WOx heterostructures. Nearly all the tips of the tungsten-oxide nanowires are capped by Zn_2SnO_4 nanocubes. Figure 7(b) shows Zn_2SnO_4 nanocubes with the size ~200 nm that prefer to nucleate and grow on the tips of the WOx nanowires, similar to the epitaxial growth of hexagonally-shaped ZnO nanostructures on the tips of WOx nanowires from Case 1.

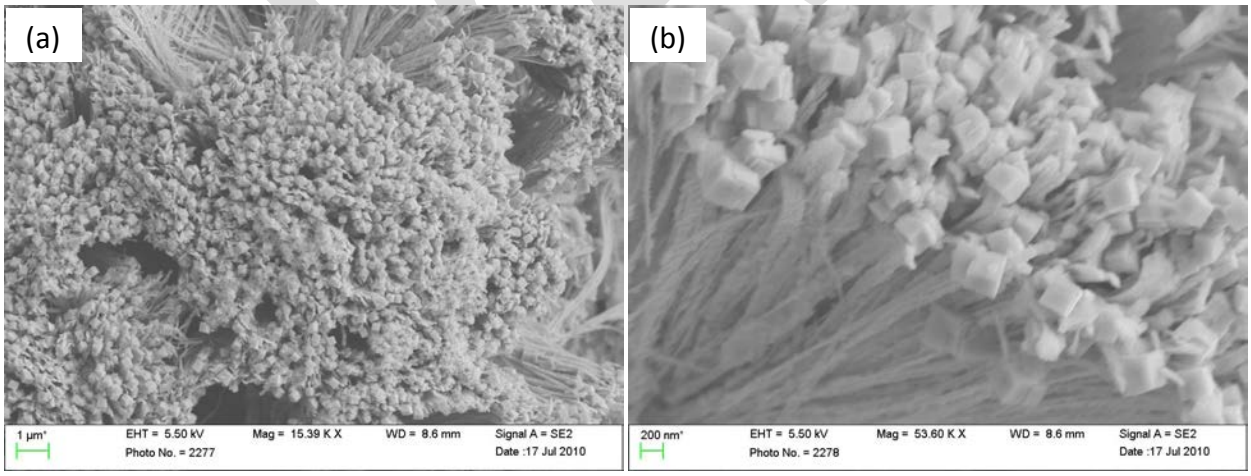

Figure 7. FESEM images of as-produced Zn_2SnO_4/WOx heterojunctions. (a) Low magnification image showing abundance of as-grown Zn_2SnO_4/WOx heterostructures. (b) High magnification image showing the side view of Zn_2SnO_4/WOx heterostructures. The $WO_{2.9}$ nanowires are capped by cubic Zn_2SnO_4 nanoparticles with the size of around 200 nm.

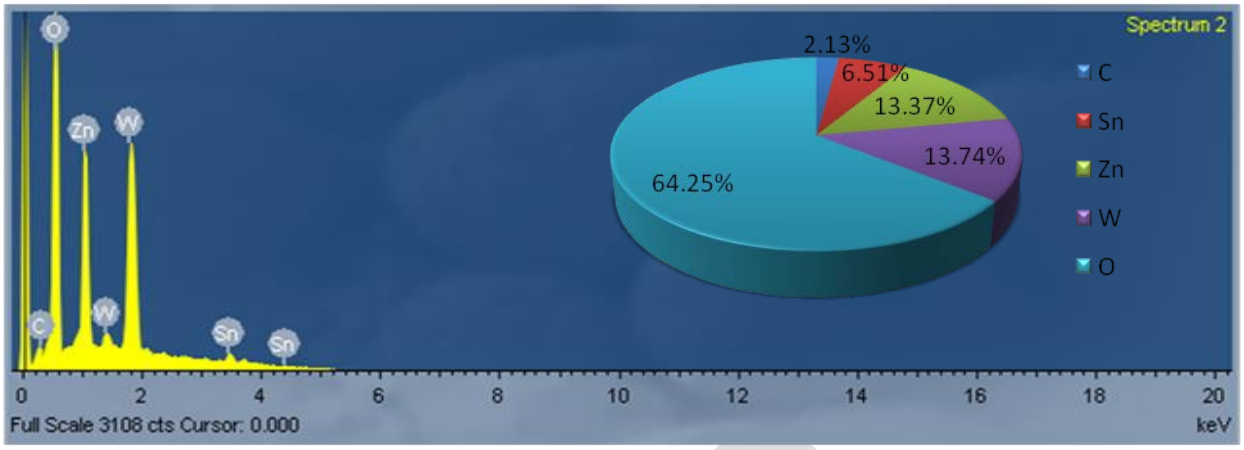

Figure 8. EDS spectrum of as-grown Zn_2SnO_4/WOx heterojunctions along with atomic ratio of C, Sn, Zn, W and O (inserted).

A typical EDS spectrum of as-prepared Zn_2SnO_4/WO_x heterostructures is given in Fig. 8, showing the presence of element oxygen (O), tungsten (W), zinc (Zn), and tin (Sn), along with a small amount of carbon (C), with atomic ratios of 64.25%, 13.74%, 13.37%, 6.51%, and 2.13%, respectively. The atomic ratio of Zn to Sn is fittingly ~2.05.

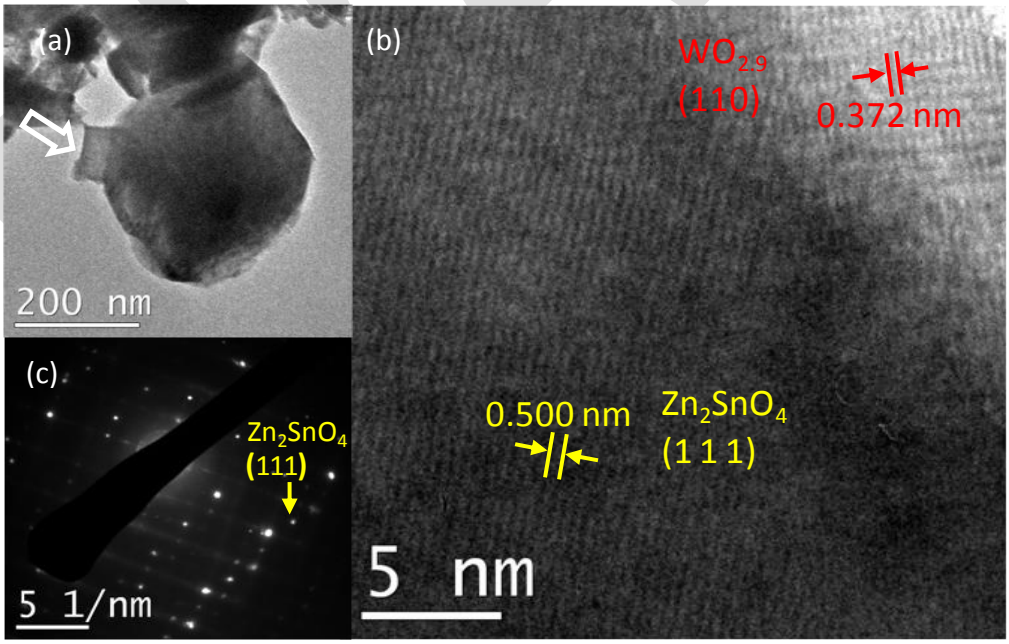

Figure 9. (a) Typical side-view low magnification TEM image of as-synthesized Zn_2SnO_4/WOx heterojunction. (b) HRTEM image of the Zn_2SnO_4/WOx heterojunction. (c) Selected area electron diffraction pattern (SAED) of Zn_2SnO_4/WOx heterojunction.

Figure 9(a) shows a side-view low-magnification TEM micrograph of an as-synthesized $Zn_2SnO_4/WO_{2.9}$ heterojunction. As indicated by the arrow, a tungsten-oxide nanowire has broken, during the TEM sample preparation, with a stem remaining, on which a Zn_2SnO_4 nanocube has been epitaxially grown. From the HRTEM micrograph (Fig. 9(b)), the lattice mismatch between $WO_{2.9}$ (110) planes (lattice fringes of 0.372 nm) and Zn_2SnO_4 (111) planes (lattice fringes of 0.500 nm) is 34.4%, which is even larger than the 22.8% for ZnO (100)/$WO_{2.9}$ (110). However, only slight stacking faults are observed at the interface region between Zn_2SnO_4 and $WO_{2.9}$. The results seem to confirm that atomically sharp interfaces at heterojunctions can be formed between different nanomaterials with large lattice mismatches, which usually cannot be obtained in their bulk counterparts [1, 25 ,27].

We hypothesize that the formation of $Zn_2SnO_4/WO_{2.9}$ heterojunctions is governed by the self-assembly and SS mechanisms. The Zn and Sn related precursors diffuse to the tips of the $WO_{2.9}$ nanowires and nucleate as Zn_2SnO_4 nanostructures. Further crystallization of cubic Zn_2SnO_4 along the <111> direction is most likely promoted under the supersaturated conditions. As shown in Fig. 9(c), the indexed SAED pattern with *d*-spacing of 4.97 Å matches well with the {111} planes of the cubic phase (space group Fd3m) of Zn_2SnO_4 (PDF card NO. 02-4234). The lattice spacing of the (111) plane of Zn_2SnO_4 is shown in the HRTEM micrograph of Fig. 9(b).

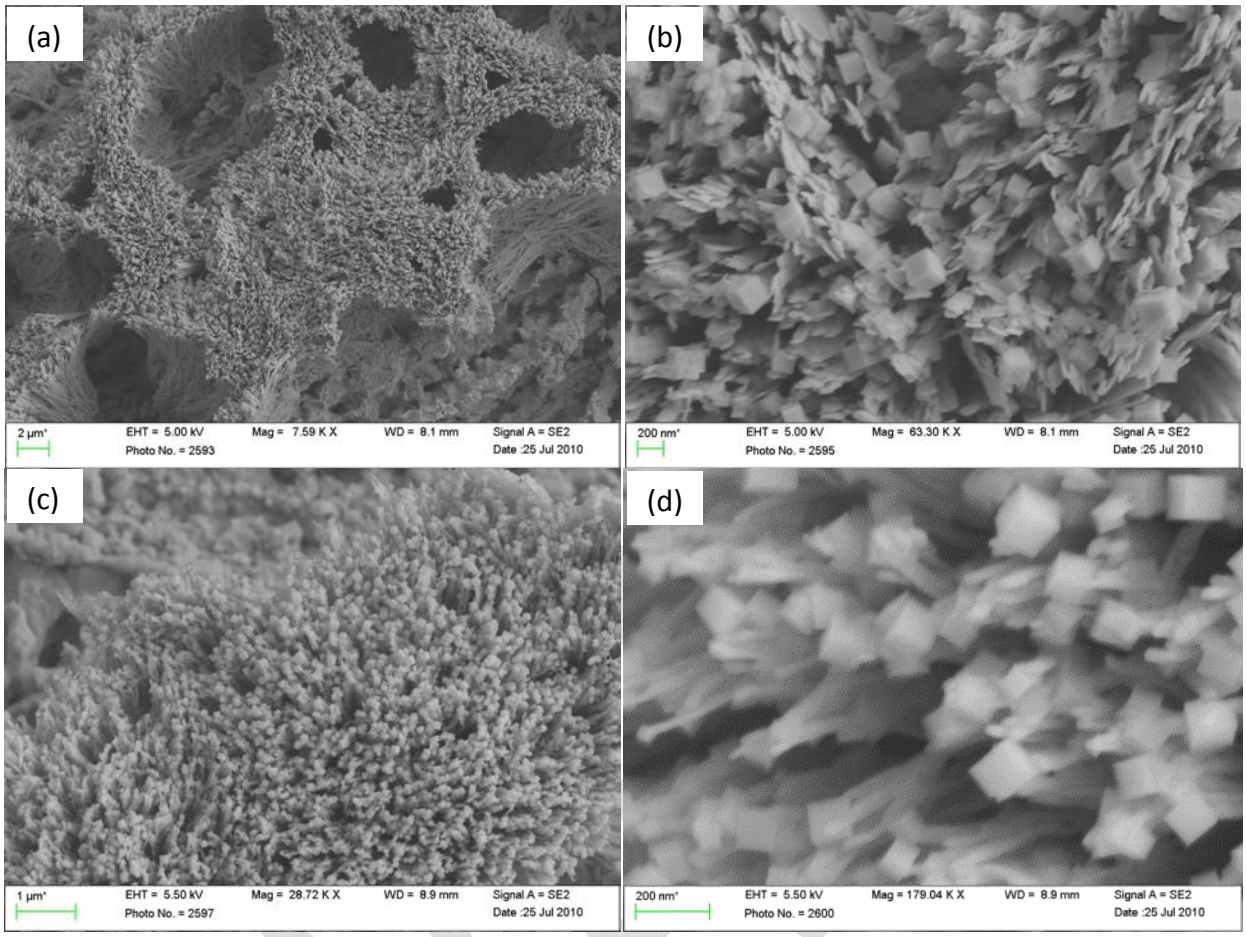

Figure 10. FESEM images of the Zn_2SnO_4/WO_x heterostructures. (a, b) Low magnification and high magnification images for case 3 showing abundance of as-grown heterostructures with the cubic particle size of ~200 nm. (c, d) Low magnification and high magnification images for case 4 showing abundance of as-grown heterostructures with the cubic particle size of ~100 nm.

Tin chloride dihydrate is added continuously into the solvent containing ethylenediamine (0.005 M) to tune the composition of the solution. As shown in Table 1, the molar concentrations are 0.004 M and 0.001 M for $Zn(NO_3)_2{\cdot}6H_2O$ and $SnCl_2{\cdot}2H_2O$, respectively, i.e. Case 3. In Case 4, the mole concentrations are 0.003 M and 0.002 M for $Zn(NO_3)_2{\cdot}6H_2O$ and $SnCl_2{\cdot}2H_2O$, respectively. The FESEM images in Fig. 10(a, b) and Fig. 10(c, d) display the results for Case 3 and Case 4, respectively. The yield of as-grown Zn_2SnO_4/WOx heterojunctions is still very high; and epitaxial growth of Zn_2SnO_4 nanocubes on the tips of

tungsten-oxide nanowires is easily identified from the high-magnification FESEM images (Fig. 10(b, d)). The size of Zn_2SnO_4 nanocubes from Case 4 is measured to be ~100 nm, smaller than the ~200 nm for Cases 2 and 3. The size of Zn_2SnO_4 nanocubes (20 to 1500 nm) may be determined by the type of alkaline mineralizers due to the solubility of Zn_2SnO_4 in different alkalines [36]. Here, the size of as-synthesized Zn_2SnO_4 nanocubes could be governed by the ratio of Zn to Sn ions, i.e. 10, 4, and 1.5 for Cases 2, 3, and 4, respectively. For Cases 2 and 3, with the ratio of Zn to Sn higher than 2, the average size of nanocubes is ~200 nm. With the ratio lower than 2, the average size of nanocubes suddenly drops to 100 nm. A higher concentration of reactants causes faster diffusion of reactants for crystal growth.

Zn_2SnO_4 nanocubes on the lateral surfaces of WOx nanowires(Cases 5, 6)

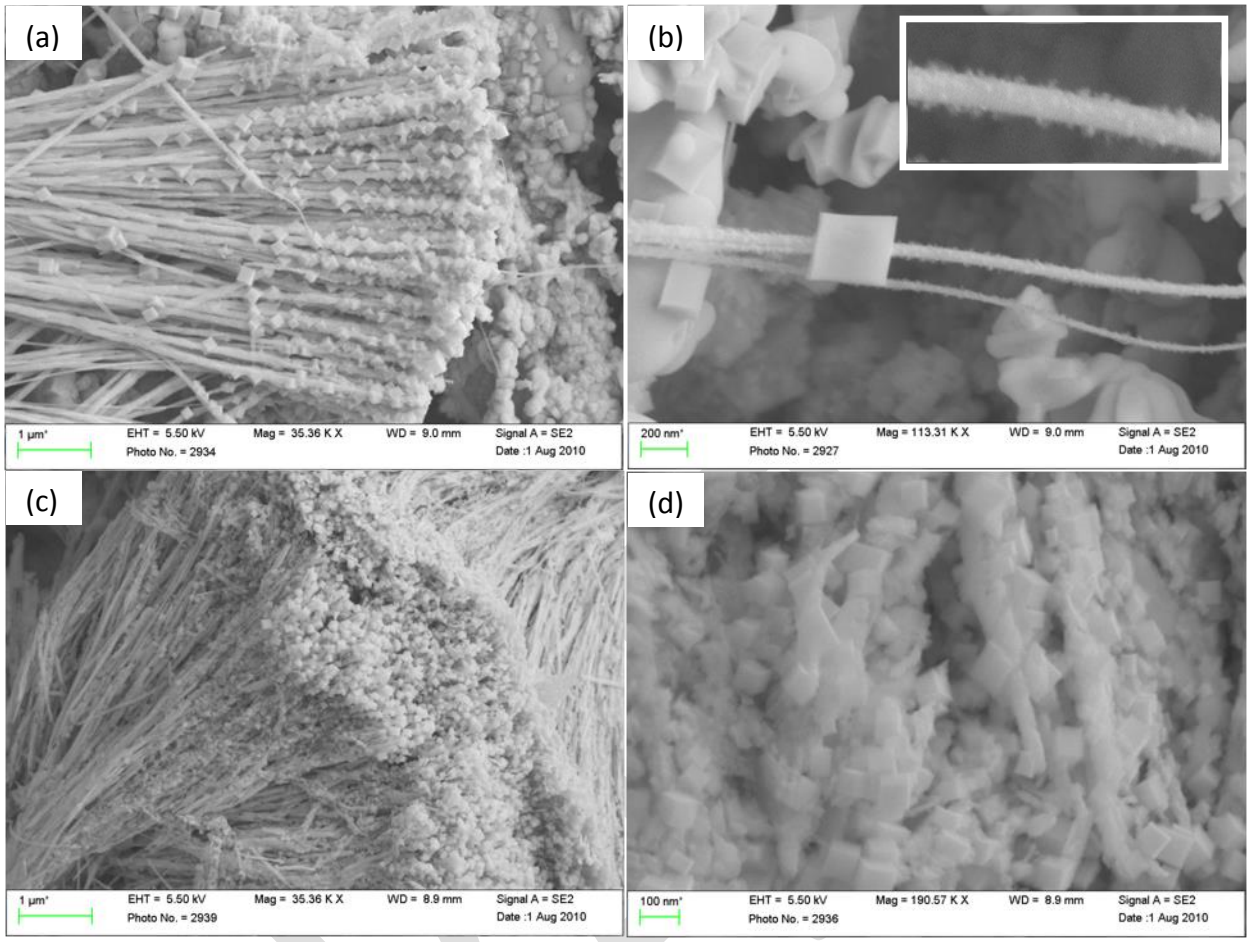

Figure 11. FESEM images of the Zn_2SnO_4/WO_x heterostructures. (a, b) Low magnification and high magnification images for case 5 showing abundance of as-grown heterostructures. (c, d) Low magnification and high magnification images for case 6 showing abundance of as-grown heterostructures.

For Case 5, as shown in Table 1, the molar concentrations are 0.002 M and 0.003 M, for $Zn(NO_3)_2{\cdot}6H_2O$ and $SnCl_2{\cdot}2H_2O$, respectively. For Case 6, the molar concentrations are 0.001 M and 0.004 M, for $Zn(NO_3)_2{\cdot}6H_2O$ and $SnCl_2{\cdot}2H_2O$, respectively. With increasing Zn ion concentration, the as-formed Zn_2SnO_4 nanocubes are found not only on the tips of the tungsten-oxide nanowires but also along on the lateral surfaces of the nanowires, as seen in the FESEM images of Figure 11. The yield of as-grown Zn_2SnO_4 nanostructures is higher than that for Cases 2-4, since the nanocubes are found both on the tips and lateral surface of the tungsten oxide nanowires, as seen from the high-magnification FESEM images (Fig. 11 (b, d)). The

characteristic size of the Zn_2SnO_4 nanocubes in Case 6 is also smaller at <50 nm, which may be caused by low concentration of Zn_2SnO_4 in the solution. The growth morphology observed in Fig. 11 seems to indicate heterogeneous growth of the nanocubes on the nanowires rather than homogenous nucleation in the solution with subsequent deposition on the nanowires. For example, Fig. 11(b) shows a nanocube with a nanowire running through it. As such, compared with Cases 1-4 where nanostructures grow on the tips of WOx nanowires, the growth of nanocubes (in Cases 5 and 6) on the lateral surface of nanowires may be due to the presence of more nucleation sites. Considerable amount of tiny nanoparticles (with size <10 nm) can be found on the surface of WOx nanowires, as shown in the inserted image of Fig. 11(b), which could play a role in serving as nucleation sites for the growth of the nanocubes. As the ratio of Zn to Sn reduces to 0.7 (Case 5) and 0.25 (Case 6), the additional Sn-related species may affect nucleation conditions. As reported by Fang et.al [17], the as-produced materials are SnO_2 and Zn_2SnO_4 when the ratio of Zn to Sn is 0.43, by using NaOH as the mineralizer under hydrothermal conditions. So, it is possible that the tiny nanoparticles found in Fig. 11(b) are SnO_2. The full understanding of the as-synthesized Zn_2SnO_4/WOx heterojunctions in Case 5 and 6 is still not very clear. However, Equation (5) may take place due to the excess amount of Sn-related species, leading to the formation of more thermodynamically active nucleation cites on the surface of WOx nanowires. Subsequently, the Zn_2SnO_4 can grow on the surface of the WOx nanowires driven by the self-assembly and SS mechanisms as described before. As can be seen from Fig. 11(b) and (d), the distribution of nanocubes becomes denser as the ratio of Zn to Sn decreases from 0.7 to 0.25, indicating that the amount of favorable nucleation sites on the surface of WOx nanowires increases with increasing the ratio of Sn to Zn.

Coaxial film of SnO_2 nanoparticles on WOx nanowires (Cases 7, 8)

The concentration of tin chloride dihydrate is continuously increased by decreasing the concentration of zinc nitrate, in Cases 7 and 8. As shown in Table 1, for Case 7, the molar concentrations are 0.0005 M and 0.005 M, for $Zn(NO_3)_2{\cdot}6H_2O$ and $SnCl_2{\cdot}2H_2O$, respectively, corresponding to a Zn to Sn ratio of 0.1. For Case 8, the molar concentrations are 0 M and 0.005 M, for $Zn(NO_3)_2{\cdot}6H_2O$ and $SnCl_2{\cdot}2H_2O$, respectively, corresponding to a Zn to Sn ratio of 0. The FESEM images in Fig. 12(a, b) and Fig. 12(c, d) show the resulting morphologies for Cases 7 and 8, respectively. Different from the previous cases, nanocubes are no longer found on the tungsten-oxide nanowires. Instead, the high-magnification FESEM (Fig. 12(b, d)) indicates a uniform deposition of material, where that the average diameter of the nanowires increases to ~70 nm and ~120 nm for Cases 7 and 8, respectively. EDS (Fig. 13) shows the presence of elemental oxygen (O), tin (Sn), and tungsten (W), along with a small amount of carbon (C). Again, the carbon is probably deposited on the surface of the WOx nanowires during synthesis of from residue in the solution. Thus, the main product from the solution synthesis is tin oxide rather than ZnO or Zn_2SnO_4 as the ratio of Zn to Sn (0.1 for this work) decreases below a critical value. As indicated by Fang et.al [17], the main products become SnO_2 as the ratio of Zn to Sn decreases to 0.25. Reaction 5 may be the main reaction during the synthesis process.

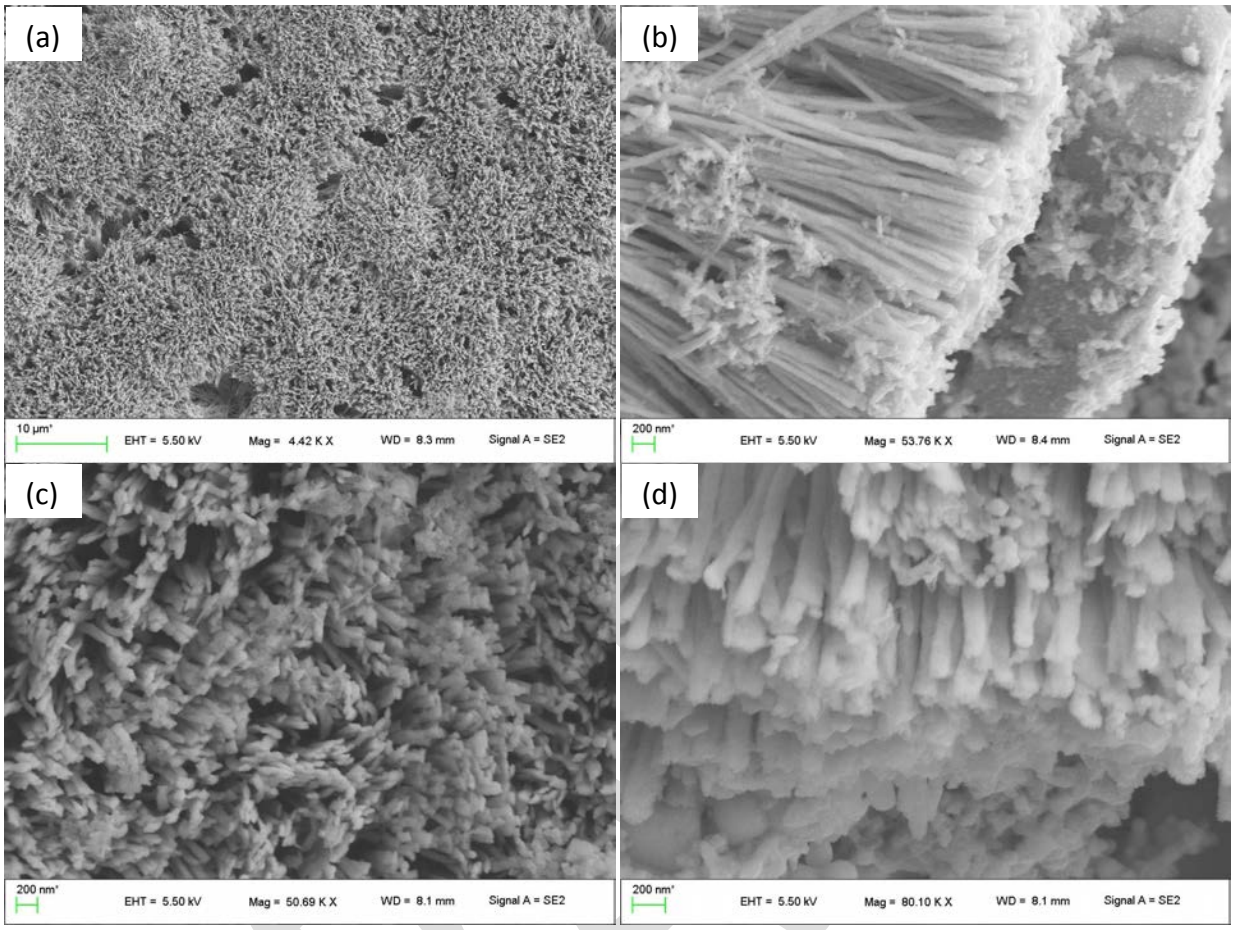

Figure 12. FESEM images of the SnO_2/WO_x heterostructures. (a, b) Low magnification and high magnification images for case 7 showing abundance of as-grown heterostructures. (c, d) Low magnification and high magnification images for case 8 showing abundance of as-grown heterostructures.

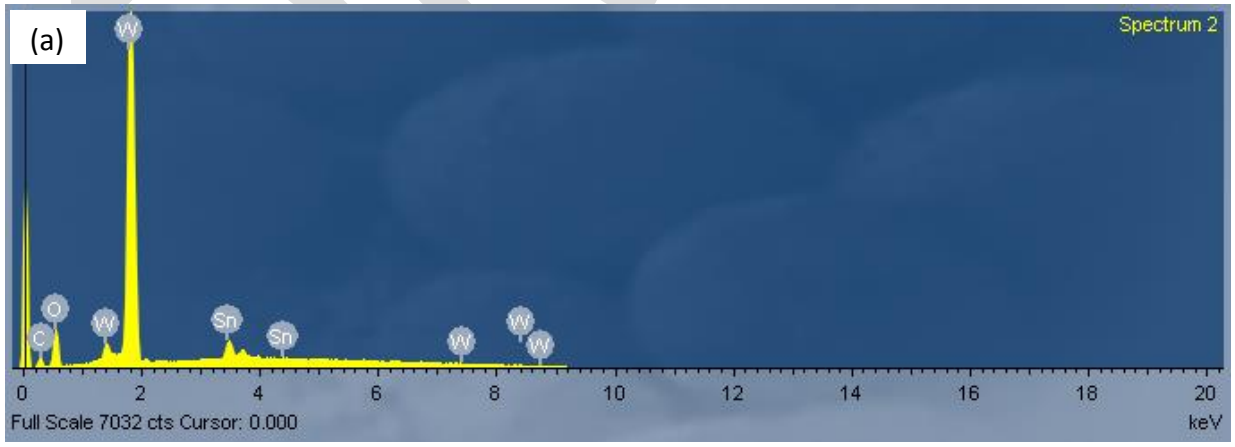

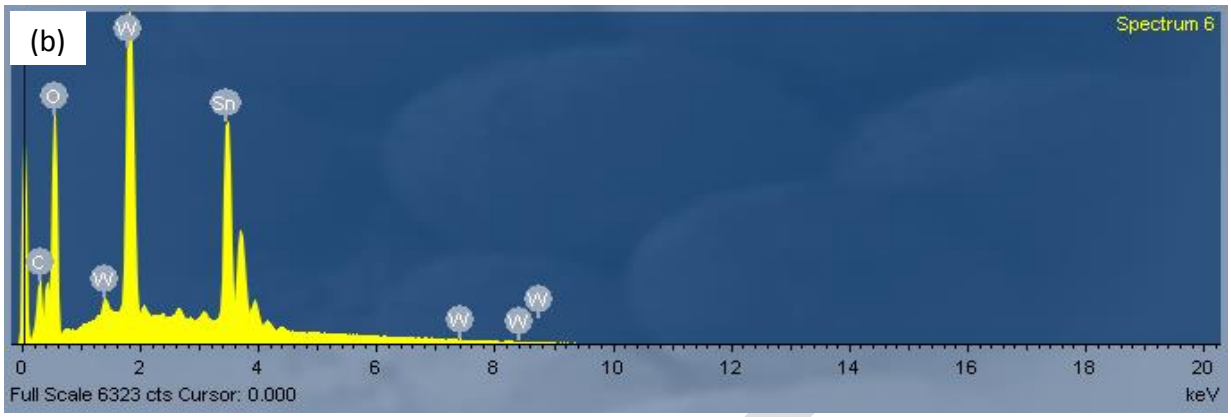

Figure 13. (a) EDS spectrum of as-grown SnO_2/WOx heterojunctions for case 7. (b) EDS spectrum of as-grown SnO_2/WOx heterojunctions for case 8.

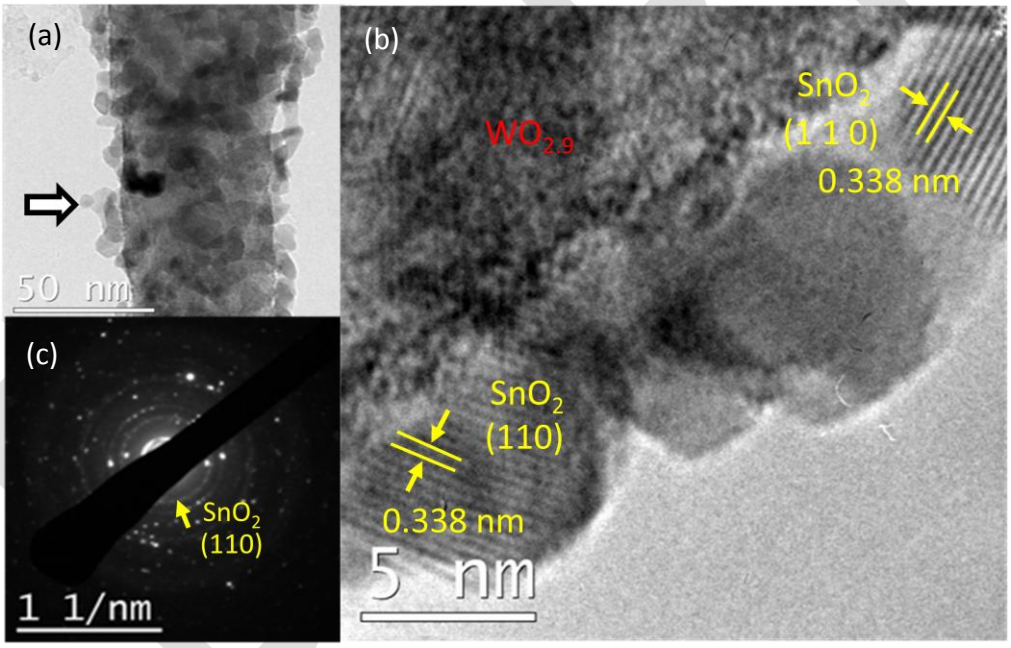

Figure 14. (a) Typical side-view low magnification TEM image of as-synthesized SnO_2/$WO_{2.9}$ heterojunction for case 7. (b) HRTEM image of the SnO_2/$WO_{2.9}$ heterojunction for case 7. (c) Selected area electron diffraction pattern (SAED) of SnO_2/$WO_{2.9}$ heterojunction for case 7.

TEM (Fig. 14(a)) reveals that the coating on the tungsten-oxide nanowires is actually a nanoparticle film. The measured d-spacing (3.38 Å) of the (110) plane for the nanoparticles matches very well with the tetragonal phase of SnO_2 (PDF card NO. 00-9163). In Fig. 14(c), the

indexed SAED pattern, with the first three highest intensities of 3.35, 2.65, and 1.74 Å, agrees well with the tetragonal phase (space group P42/mnm) of SnO_2 (PDF card NO. 00-9163). The d-spacings correspond to {110}, {101}, and {211}, respectively. The measured average size of the as-synthesized SnO_2 nanoparticles is ~6-7 nm, which matches very well with the diameter increase of the nanowires (shown in FESEM) from ~50 nm to ~70 nm (for Case 7). As a result, the Sn-related species tend to nucleate on the surface of the tungsten-oxide nanowires leading to a uniform coating of SnO_2 nanoparticles. For Case 8, more nanoparticles are deposited on the tungsten-oxide nanowires, leading to larger diameter increase (~120 nm versus ~70 nm for Case 7). With only tin precursor in the solution, the obtained nanomaterials are SnO_2/WOx heteronanostructures.

As can be seen from the low-magnification TEM micrograph, some of the SnO_2 nanoparticles stack on the inner layer of SnO_2 nanoparticles, forming double layered coatings of SnO_2 nanoparticles on the surface of the tungsten-oxide nanowire, as shown by the arrow in Fig. 14(a). Furthermore, the as-grown SnO_2 nanoparticles possess irregular shapes. The formation of SnO_2 nanoparticles seems to be very quick, leading to the production of considerable amounts of SnO_2 particles in a short amount of time. The second layer of SnO_2 nanoparticles may be homogeneously formed in the solution, which then deposits on the first layer of SnO_2 nanoparticles. As can be seen from Fig. 14(b), the HRTEM micrograph of the interface between a $WO_{2.9}$ nanowire and SnO_2 nanoparticles clearly shows the deposition of irregular shaped SnO_2 nanoparticles on the surface of $WO_{2.9}$ nanowire.

Solution Synthesis when no WOx nanowire scaffold nanowires are present

Synthesis of uniform film

Concluding Remarks

In this work, hexagonal ZnO nanoplates, Zn_2SnO_4 nanocubes, and SnO_2 nanoparticle films are grown on tungsten-oxide nanowiresvvia a two-step synthesis process combining flame-based and solution-based methods. We hypothesize that the formation of as-grown heterojunctions is governed by self-assembly and SS mechanisms. Under certain conditions, the tips of tungsten-oxide nanowires serve as ideal thermodynamically active nucleation sites for the synthesis of various secondary nanomaterials. Epitaxial growth of hexagonal ZnO nanoplates on the ends of tungsten oxide nanowires takes place when only Zn precursor exists in the solution. On the other hand, fine uniform coating of SnO_2 nanoparticles on the surface of tungsten-oxide naowires are obtained when only Sn precursor is in the solution. It is possible that the formation of fine irregular shaped SnO_2 nanoparticles is much faster than that of ZnO leading to the formation core/shell $WO_{2.9}/SnO_2$ nanowires. By decreasing the ratio of Zn to Sn, epitaxial growth of Zn_2SnO_4 nanocube/$WO_{2.9}$ nanowire heterojunction can change to radial growth of cubic Zn_2SnO_4 nanocube/$WO_{2.9}$ nanowire heterojunction on the lateral surfaces of the nanowire. The results reveal that the concentration of Sn-related precursors affects the distribution of available nucleation sites for the growth of Zn_2SnO_4 nanocubes. As the ratio of Sn to Zn increases, more nucleation sites tend to be formed on the surface of tungsten oxide nanowire,s resulting in radial growth of Zn_2SnO_4 nanocube/$WO_{2.9}$ nanowire heterojunction. Furthermore, the combined flame and solution synthesis process shows a promising technique for the fabrication of defect-free interface of heterostructured nanomaterials with relatively large lattice mismatches in the future.

Acknowledgements

This work was supported by the Army Research Office (Grant W911NF-08-1-0417) and the National Science Foundation (Grant CBET 0755615).

Reference

[1] Aneta J. Mieszawska, Romaneh Jalilian, Gamini U. Sumanasekera, and Francis P. Zamborini. The synthesis and fabrication of one-dimensional nanoscale heterojunctions. Small, 2007; 3: 722-756.

[2] Yue Wu, Jie Xiang, Chen Yang, Wei Lu, Charles M. Lieber. Single-crystal metallic nanowires and metal/semiconductor nanowire heterostructures. Nature, 2004; 430:61-65.

[3] Delia J. Milliron, Steven M. Hughes, Yi Cui, Liberato Manna,Jingbo Li, Lin-Wang Wang, A. Paul Alivisatos. Colloidal nanocrystal heterostructures with linear and branched topology. Nature 2004; 430:190-195.

[4] Sven Barth, Francisco Hernandez-Ramirez, Justin D. Holmes, Albert Romano-Rodriguez. Synthesis and applications of one-dimensional semiconductors. Progress in Materials Science, 2010; 55: 563-627.

[5] Lian Ouyang, Kristin N. Maher, Chun Liang Yu, Justin McCarty, and Hongkun Park. Catalyst-Assisted Solution-Liquid-Solid Synthesis of CdS/CdSe Nanorod Heterostructures. J. AM. CHEM. SOC. 2007; 129:133-138.

[6] Dong-Feng Zhang, Ling-Dong Sun, Chun-Jiang Jia, Zheng-Guang Yan, Li-Ping You, and Chun-Hua Yan. Hierarchical Assembly of SnO2 Nanorod Arrays on r-Fe2O3 Nanotubes: A Case of Interfacial Lattice Compatibility. J. AM. CHEM. SOC. 2005; 127:13492-13493.

[7] Yunho Baek, Yoonho Song, Kijung Yong. A novel heteronanostructure system: hierarchical W nanothorn arrays on WO3 nanowhiskers. Adv. Mater. 2006; 18:3105-3110.

[8] Guozhen Shen, Di Chen, and Chongwu Zhou. One-step thermo-chemical synthetic method for nanoscale one-dimensional heterostructures. Chem. Mater., 2008; 20: 3788-3790.

[9] Hyeyoung Kim, Youngjo Tak, Karuppanan Senthil, Jinmyoung Joo, Sangmin Jeon, Kijung Yong. Novel heterostructure of CdS nanoparticle/WO3 nanowhisker: Synthesis and photocatalytic properties. J. Vac. Sci. Technol. B 2009; 27:2182-2186.

[10] Shashwati Sena, Prajakta Kanitkarb, Ankit Sharmac, et al. Growth of SnO2/W18O49 nanowire hierarchical heterostructure and their application as chemical sensor. Sensors and Actuators B 2010; 147:453-460.

[11] Elias de Barros Santos, Juliana Martins de Souza e Silva, Fernando Aparecido Sigoli, Italo Odone Mazali. Size-controllable synthesis of functional heterostructured TiO2-WO3 core-shell nanoparticles. J. Nanopart. Res., 2011; 13: 5909-5917.

[12] M.A. Gondal, A.Bagabas, A. Dastageer, A. Khalil. Synthesis, characterization, and antimicrobial application of nano-palladium-doped nano-WO3. Journal of Molecular Catalysis A: Chemical. 2010; 323: 78-83.

[13] Dong-Feng Zhang, Ling-Dong Sun, Jia-Lu Yin, Chun-Hua Yan. Low-temperature fabrication of highly crystalline SnO2 Nanorods. Adv. Mater. 2003; 15:1022-1025.

[14] Benjamin Weintraub, Yulin Deng, and Zhong L. Wang. Position-controlled seedless growth of ZnO nanorod arrays on a polymer substrate via wet chemical synthesis. J. Phys. Chem. C. 2007; 111:10162-10165.

[15] Jae-Min Jang, Jin-Yeol Kim, Woo-Gwang Jung. Synthesis of ZnO nanorods on GaN epitaxial layer and Si (100) substrate using a simple hydrothermal process. Thin Solid Films. 2008; 516:8524-8529.

[16] N O V Plank, H J Snaith, C Ducati, J S Bendall, L Schmidt-Mende and M E Welland. A simple low temperature synthesis route for ZnO-MgO core-shell nanowires. Nanotechnoloty. 2008; 19:465603.

[17] Jun Fang, Aihong Huang, Peixu Zhu, Ningsheng Xu, Jianqin Xie,Junsheng Chi, Shouhua Feng, Ruren Xu, Mingmei Wu. Hydrothermal preparation and characterization of Zn2SnO4 particles. Materials Research Bulletin. 2001; 36: 1391–1397.

[18] Xianliang Fu, Xuxu Wang, Jinlin Long, Zhengxin Ding, Tingjiang Yan, Guoying Zhang, Zizhong Zhang, Huaxiang Lin, Xianzhi Fu. Hydrothermal synthesis,characterization,and photocatalytic properties of Zn2SnO4. Journal of Solid State Chemistry. 2009; 182:517-524.

[19] Fusheng Xu, Stephen D. Tse, Jafar F. Al-Sharab, Bernard H. Kear. Flame synthesis of aligned tungsten oxide nanowires. Appl. Phys. Lett. 2006; 88:243115.

[20] Hou T. Ng, Jun Li, Michael K. Smith, Pho Nguyen, Alan Cassell, Jie Han, M. Meyyappan. Growth of epitaxial nanowires at the junctions of nanowalls. Sience, 2003; 300: 1249.

[21] Michael H. Huang, Samuel Mao, Henning Feick, Haoquan Yan, Yiying Wu, Hannes Kind, Eicke Weber, Richard Russo, Peidong Yang. Room-temperature ultraviolet nanowire nannolasers. Science, 2001; 292: 1897-1899.

[22] Timothy J. Trentler, Kathleen M. Hickman, Subhash C. Goel, Ann M. Viano, Patrick C. Gibbons, William E. Buhro. Solution-liquid-solid growth of crystalline III-V semiconductors: An analogy to vapor-liquid-solid growth. Science, 1995; 270: 1791-1794.

[23] Brent A. Wacaser, Kimberly A. Dick, Jonas Johansson, Magnus T. Borgstrom, Knut Deppert, and Lars Samuelson. Preferential interface nucleation: an expansion of the VLS growth mechanism for nanowires. Adv. Mater., 2009; 21: 153-165.

[24] Xueyun Gao, Tao Gao and Lide Zhang. Solution-solid growth of α-monoclinic selenium nanowires at room temperature. J. Mater. Chem., 2003; 13: 6-8.

[25] Zhores I. Alferov. The history and future of semiconductor heterostructures. Semiconductors, 1998; 32: 1-14.

[26] R. S. Wagner and W. C. Ellis. Vapor-liquid-solid mechanism of single crystal growth. Applied Physics Letters. 1964, 4: 89-90.

[27] Guozhen Shen, Di Chen, and Chongwu Zhou. One-step thermo-chemical synthetic method for nanoscale one-dimensional heterostructures. Chem. Mater., 2008; 20: 3788-3790.

[28] S.A. Oliver, H.H. Hamdeh, and J.C. Ho. Localized spin coating in partially inverted ZnFe2O4 fine powders. Physical Review B,1999; 60: 5.

[29] Sanjay Mathur, Stenfan Hufner, Robert Haberkorn, Mohammad Jilavi, et.al. Single-source sol-gel synthesis of nanocrystalline ZnAl2O4: Structural and optical properties. Journal of the American Ceramic Society. 2001; 84: 1921-28.

[30] Kurt E. Sickafus, John M. Wills and Norman W. Grimes. Structure of spinel. J. Am. Ceram. Soc., 1999; 82: 3279-92.

[31] Qilian Dai, Jiajun Chen, Liyou Lu, Jinke Tang, and Wenyong Wang. Plulsed laser deposieion of CdSe quantum dots on Zn2SnO4 nanowires and their photovoltaic applications. Nano Lett., 2012; 12: 4187-4193.

[32] Bing Tan, Elizabeth Toman, Yanguang Li, and Yiying Wu. Zinc Stannate (Zn2SnO4) dye-sensitized solar cells. J. AM. CHEM. SOC., 2007; 129: 4162-4163.

[33] Maolin Zhang, Taicheng An, Xiaohong Wu, Cun Wang, Guoying Sheng, Jiamo Fu. Preparation and photocatalytic properties of a nanometer ZnO-SnO2 coupled oxide. Applied Catalysis A: General, 2004; 260: 215-222.

[34] A. Rong, X.P. Gao, G.R.Li, T.Y. Yan, H.Y. Zhu, J.Q. Qu, D.Y. Song. Hydrothemal synthesis of ZnSnO as anode materials for Li-ion battery. J. Phys. Chem. B, 2006; 110: 14754-14760.

[35] J.H. Yu, G.M. Choi. Current-voltage characteristics and selective CO detection of ZnSNO and ZnO/ZnSnO4, SnO2/ZnSnO4 layered-type sensors. Sensors and Acuators B: Chemical, 2001; 72: 141-148.

[36] Yaqi Jiang, Xiaoxia Chen, Ran Sun, Zhao Xiong, Lansun Zheng. Hydrothermal syntheses and gas sensing properties of cubic and quasi-cubic Zn2SnO4. Materials Chemistry and Physics, 2011; 129: 53-61.